Geophysical Journal International

Geophys. J. Int. (2018) **212,** 244–263
Advance Access publication 2017 October 3
GJI Marine geosciences and applied geophysics

doi: 10.1093/gji/ggx415

Resolving the fine-scale velocity structure of continental hyperextension at the Deep Galicia Margin using full-waveform inversion

R.G. Davy,[1,2] J.V. Morgan,[2] T.A. Minshull,[1] G. Bayrakci,[1] J.M. Bull,[1] D. Klaeschen,[3] T.J. Reston,[4] D.S. Sawyer,[5] G. Lymer[4] and D. Cresswell[4]

[1]*Ocean and Earth Science, University of Southampton, Southampton SO*17 1*BJ, United Kingdom*
[2]*Department of Earth Science and Engineering, Imperial College London, London SW*7 2*AZ, United Kingdom. E-mail: r.davy@imperial.ac.uk*
[3]*GEOMAR Helmholtz Centre for Ocean Research, D-*24148 *Kiel, Germany*
[4]*University of Birmingham, Birmingham B*15 2*TT, United Kingdom*
[5]*RICE University, Houston, TX* 77005*, USA*

Accepted 2017 September 27. Received 2017 September 22; in original form 2017 April 5

SUMMARY

Continental hyperextension during magma-poor rifting at the Deep Galicia Margin is characterized by a complex pattern of faulting, thin continental fault blocks and the serpentinization, with local exhumation, of mantle peridotites along the *S*-reflector, interpreted as a detachment surface. In order to understand fully the evolution of these features, it is important to image seismically the structure and to model the velocity structure to the greatest resolution possible. Traveltime tomography models have revealed the long-wavelength velocity structure of this hyperextended domain, but are often insufficient to match accurately the short-wavelength structure observed in reflection seismic imaging. Here, we demonstrate the application of 2-D time-domain acoustic full-waveform inversion (FWI) to deep-water seismic data collected at the Deep Galicia Margin, in order to attain a high-resolution velocity model of continental hyperextension. We have used several quality assurance procedures to assess the velocity model, including comparison of the observed and modeled waveforms, checkerboard tests, testing of parameter and inversion strategy and comparison with the migrated reflection image. Our final model exhibits an increase in the resolution of subsurface velocities, with particular improvement observed in the westernmost continental fault blocks, with a clear rotation of the velocity field to match steeply dipping reflectors. Across the *S*-reflector, there is a sharpening in the velocity contrast, with lower velocities beneath *S* indicative of preferential mantle serpentinization. This study supports the hypothesis that normal faulting acts to hydrate the upper-mantle peridotite, observed as a systematic decrease in seismic velocities, consistent with increased serpentinization. Our results confirm the feasibility of applying the FWI method to sparse, deep-water crustal data sets.

Key words: Atlantic Ocean; Waveform inversion; Seismic tomography; Continental tectonics: extensional.

1 INTRODUCTION

In recent years, there has been an increase in the availability of high-density seismic data sets and a significant increase in the power of computers. These combined factors have enabled a broadening application of seismic full-waveform inversion (FWI). FWI provides a powerful extension of popular seismic traveltime tomography methods, with the ability to resolve subsurface velocity structure to half the seismic wavelength, which can be an order of magnitude smaller than possible with traveltime tomography for a typical crustal target (Wu & Toksöz 1987; Williamson 1991; Virieux & Operto 2009). 3-D FWI has yielded impressive results on marine seismic data sets, producing high-resolution velocity models which can be used directly for geological interpretation or for the migration of reflection seismic data to produce detailed images (e.g. Sirgue *et al.* 2010; Ratcliffe *et al.* 2011; Jones *et al.* 2013; Mispel *et al.* 2013; Mothi *et al.* 2013; Warner *et al.* 2013). The vast majority of such studies have utilized seismic data recorded on either hydrophone streamers or ocean bottom cables (OBC), in relatively shallow marine environments (water depth < 1000 m). Both hydrophone streamers and OBC possess a high density of receivers, enabling dense sampling of the subsurface for the FWI process (Warner *et al.* 2013).

However, the maximum depth of investigation for these methods is restricted to approximately a third to a sixth of the maximum source–receiver offset, limiting their use for studies of crustal-scale targets or those in deep-water environments (Warner *et al.* 2010; Morgan *et al.* 2013).

These limitations can be overcome in deep-water environments by applying FWI to wide-angle seismic data sets recorded by ocean bottom seismometers and hydrophones (OBS/H). A limited number of studies have previously applied FWI to OBS/H data sets. Dessa *et al.* (2004) and Operto *et al.* (2006) presented the first results of frequency-domain FWI applied to OBS data, utilizing a 2-D deployment of 100 instruments at the Nankai Trough, east of Japan. The velocity structure of compressional tectonic features within the accretionary prism and the downgoing oceanic crust were resolved, where they had not previously been observed in traveltime tomographic models. Kamei *et al.* (2012) applied frequency-domain FWI to a separate deployment of 54 OBS at the Nankai trough, resolving the fine-scale velocity structure of megasplay faulting. Recently, Morgan *et al.* (2016) demonstrated the application of 3-D time-domain FWI on an array of 21 OBS situated across the Endeavour oceanic spreading centre of the Juan de Fuca Ridge, revealing low-velocity zones interpreted to represent a magmatic-hydrothermal reaction zone (Arnoux *et al.* 2017). These studies have made use of relatively dense OBS deployments (∼1 km spacing), or a 3-D seismic shooting configuration, both of which are not always possible in academic experiments. We build on these studies by applying FWI to a comparatively sparse data set (sparse OBS locations recording frequent seismic shots), in order to demonstrate the feasibility of the technique in areas where only 2-D or older data sets are available.

Here, we demonstrate the application of acoustic 2-D FWI to a sparse wide-angle data set collected on 19 OBS/H at the Deep Galicia Margin in the North Atlantic, with the aim of resolving the fine-scale velocity structure of continental hyperextension. Continental fault blocks within this hyperextended domain can possess dimensions as small as a few kilometres, beyond the limit of what is resolvable with traveltime tomography, making this an ideal target for FWI (Davy *et al.* 2016). We investigate the robustness of our FWI result by testing several parameters influencing the inversion, including the offsets and time windowing of the input data, and uncertainties in the sediment velocity model. Our result cannot be quality checked using 3-D phase plots, and so we utilize alternative quality assurances, including checkerboard tests, waveform comparisons and correlation with reflection seismic imaging. Given the nature of both the data set and our crustal target, this application of FWI provides an excellent case study to explore the practical limits of this increasingly popular technique.

2 BACKGROUND

2.1 Geological setting

Rifting at the Deep Galicia Margin (Fig. 1a) has resulted in the extreme thinning of the continental crust over distances of 100–200 km. Unaltered crust landward of the proximal rift margin is ∼30 km thick and has been thinned through a complex pattern of faulting to only a few kilometres at the distal limits of the margin (Zelt *et al.* 2003; Reston 2009). Initial extensional deformation is inferred to have occurred as high-angle normal faulting, which formed large fault-bound blocks between 10 and 20 km wide, thinning the crust to between 20 and 30 km thick (Ranero & Pérez-Gussinyé 2010). With continued extension of the margin, these continental fault blocks rotated to low angles, at which point their bounding faults locked up (Ranero & Pérez-Gussinyé 2010). The faulting mechanism responsible for how continued extension was accommodated still remains controversial. McDermott & Reston (2015) propose that the crust deformed through polyphase faulting, where new preferentially oriented normal faults overprinted existing faults and fault blocks. Ranero & Pérez-Gussinyé (2010) suggest that the continued deformation occurred as a sequential pattern of faulting, where new preferentially oriented normal faults were successively formed through the thinned crust, but did not cut the preceding fault. Both of these proposed mechanisms lead to the extreme thinning of the continental crust.

As the margin extended and thinned at an ultra-slow rate (<10 mm yr^{-1} half-spreading rate), it allowed time for the entire crust to cool conductively, resulting in the normally ductile mid- and lower crust becoming progressively embrittled (Srivastava *et al.* 2000; Pérez-Gussinyé & Reston 2001; Pérez-Gussinyé *et al.* 2003). Once the crustal thicknesses reached <10 km, the entire crust became brittle and coupled, a phenomenon known as continental hyperextension. A fully embrittled crust enabled normal faults to form through the entire crust, from the seafloor to the underlying mantle (Pérez-Gussinyé & Reston 2001; Pérez-Gussinyé *et al.* 2003; Pérez-Gussinyé 2013). These faults acted as conduits, delivering seawater to the upper mantle and forming a layer of serpentinized mantle, which is an inherently weak material (Pérez-Gussinyé & Reston 2001; Reston *et al.* 2007; Bayrakci *et al.* 2016). With continued extension these faults soled out into the structurally weak layer of mantle serpentinite, forming a large and low angle ($<20^\circ$) detachment fault, known as the *S*-reflector (Fig. 1c), which also corresponds to the crust–mantle boundary in the distal margin (Reston *et al.* 2007). It has been shown recently that these faults, which sole into the *S*-reflector, preferentially hydrate the upper mantle which results in varying degrees of mantle serpentinization, observed as a pattern of high and low *P*-wave velocities (Bayrakci *et al.* 2016; Davy *et al.* 2016). In the final stages of rifting, serpentinized subcontinental mantle was exhumed to the seafloor along the *S*-reflector, and was also emplaced west of this hyperextended domain, forming a structure known as the Peridotite Ridge (Beslier *et al.* 1993), before the onset of seafloor spreading (Davy *et al.* 2016). Sedimentation of this margin occurs at all stages of the rifting process, giving rise to pre-, syn- and post-rift sedimentary units, which are mentioned throughout our interpretations (Fig. 1d, Ranero & Pérez-Gussinyé 2010).

2.2 Seismic data set

This study investigates a 2-D subset (3-D inline 420) of the Galicia-3-D seismic experiment, which was performed at the Deep Galicia Margin, west of Spain (Fig. 1a) between 2013 June 01 and August 02 (Fig. 1b; see Davy *et al.* 2016 and Dean *et al.* 2015 for further details on the wide-angle and multichannel seismic survey parameters, respectively). Multichannel seismic reflection data were recorded by the R/V *Marcus G. Langseth* towing four streamers of ∼6 km length, spaced 200 m apart and at a depth of 15 m. Each streamer had 468 channels spaced at 12.5 m intervals. The seismic source comprised two 3300 cu.in. air gun arrays, towed at a depth of 9 m and fired alternately every 37.5 m (a shot interval of ∼16 s), optimal for high-resolution 3-D reflection imaging, but suboptimal for wide-angle studies. Processing of this reflection seismic data set was performed by Repsol, who produced a 3-D pre-stack Kirchhoff time migration. Wide-angle seismic arrivals along this 2-D profile were

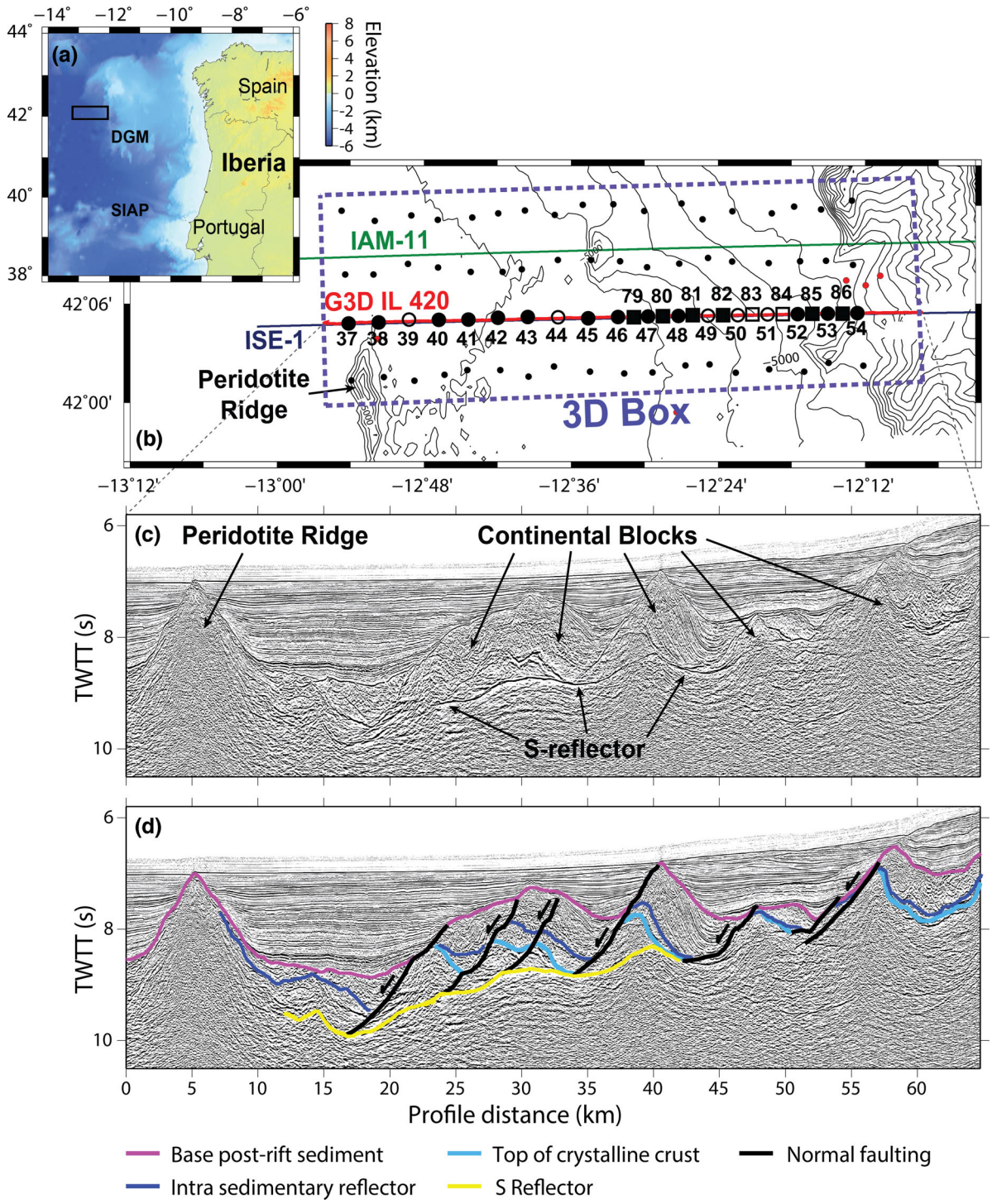

Figure 1. (a) Bathymetric map of the Deep Galicia Margin (DGM) and the Southern Iberia Abyssal Plain (SIAP) with the relative location of (b) (black rectangle). (b) Map of the Galicia-3-D seismic experiment. Galicia 3-D inline 420 seismic profile is illustrated by a red line; large black circles indicate the location of OBIF OBS along seismic inline 420; large black squares indicate GEOMAR OBH; unfilled circles and squares indicate instruments which recovered no data or were excluded from the FWI process. Purple line indicates the ISE-1 seismic profile; green line indicates the IAM-11 seismic profile and ODP Leg 103 sites are indicated by red circles (Boillot *et al.* 1987). (c) Kirchhoff pre-stack time-migrated multichannel seismic reflection image of inline 420, highlighting features of the Deep Galicia Margin. (d) Simplified interpretation of C).

recorded by 26 OBS/H from the UK Ocean Bottom Instrumentation Facility (OBIF) (Minshull *et al.* 2005) and GEOMAR (Fig. 1b). The eastern 17 OBS/H were spaced densely at ∼1.7 km intervals, with the intention to produce a high-resolution 2-D velocity models of the geological structure above and below the *S*-reflector and form the focus of this study. The western nine OBS/H, spaced at distances of ∼3.4 km, cover the Peridotite Ridge (Fig. 1c) and the sedimentary basins on its western and eastern flanks. Two of the 26 OBS/H were not retrieved, while another five instruments returned no usable data.

Most of the OBS/H in the Galicia-3-D seismic experiment recorded seismic shots with a complete azimuthal coverage, allowing these instruments to be accurately relocated by minimizing the traveltime misfit between the observed and calculated direct water-wave arrival. However, eight OBH along this line were deployed for a shorter period and only recorded shots from a single seismic profile, limiting their ability to be relocated accurately in the cross-line direction (OBH 79–86). On average each instrument was relocated by 299 m.

3 FULL-WAVEFORM INVERSION

The theory behind FWI and its application to seismic data was first developed in the 1980s by Lailly (1983) and Tarantola (1984). It was shown that finite-difference modeling of the wavefield through a starting medium, followed by a localized least-squares inversion, minimizing the misfit between observed and modeled wavefield, could be used to recover physical properties of the subsurface (Tarantola 1987). Initial applications of FWI were performed in the time domain, but were limited given the high computational demand of the method (Kolb *et al.* 1986). Three decades later and FWI is still performed based on these underlying principles, with modern codes capable of performing FWI in either the time or frequency domain, in two or three dimensions, approximating either the acoustic or elastic wave equation, and can include the effects of seismic attenuation and anisotropy (e.g. Pratt 1999; Brossier *et al.* 2009; Warner *et al.* 2013). It has also been shown that the maximum achievable resolution using these codes is on the order of half the seismic wavelength, making it superior to traveltime tomography (Virieux & Operto 2009). Although FWI can extract any physical property which affects the wave equation, it is most commonly used to determine the compressional velocity structure of the subsurface (e.g. Kapoor *et al.* 2013).

FWI requires an accurate starting model (typically derived from reflection or traveltime tomography) capable of reproducing the majority of the observed wavefield to within half a seismic cycle at the lowest inversion frequency, observed seismic data, and a derivation of a source wavelet (Virieux & Operto 2009). Forward modeling of synthetic wavefields through the starting model is achieved by solving the numerical wave equation (either acoustic or elastic) through a method of finite differences (Virieux 1986; Operto *et al.* 2007). Residual data are then calculated as the difference between the synthetic and observed data, and then the residuals are backpropagated through the velocity model and subsequently cross-correlated with the synthetic data to determine a model update (Tarantola 1984; Pratt *et al.* 1998; Virieux & Operto 2009). Iteration of this process builds an increasingly resolved velocity model, capable of reproducing the observed wavefield to greater degree. As FWI is a localized inversion method, it runs the risk of converging to a local minimum, commonly referred to as cycle skipping (Bunks *et al.* 1995; Sirgue 2006). Cycle skipping occurs when seismic arrivals in the synthetic wavefield are more than 180° out of phase with that of the observed wavefield. This results in the inversion process attempting to force a match between the observed and synthetic wavefield which is one or more cycles from the true match. In an effort to mitigate against cycle skipping, it is common practice to start FWI at long wavelengths (low frequencies), which are easier to match within half a cycle, and systematically incorporate shorter wavelengths (higher frequencies) into the modeling, commonly referred to as multiscale FWI (Bunks *et al.* 1995; Sirgue 2006). A complete description of FWI and the underlying theory can be found in Pratt *et al.* (1998) and the review paper of Virieux & Operto (2009).

In this study, we perform a 2-D time-domain, acoustic, isotropic FWI, using the codes of Warner *et al.* (2013). In this code, synthetic traces are calculated through a starting model using a finite-difference method and are subsequently scaled so that their rms amplitude matches that of their corresponding observed trace. Misfit between the respective synthetic and observed traces is calculated as the sum of squares difference for each time interval, with a misfit functional representing the misfit over all traces. As this is a time-domain code, the inversion process matches a finite bandwidth of the observed wavefield, defined by a low-pass filter in which the maximum frequency is progressively increased during the inversion. At each bandwidth, the misfit functional was minimized by an iterative gradient-based optimization, which perturbed an input velocity model in order to match the calculated synthetic and respective observed traces, based on the phase shape and relative amplitude of individual arrivals. The code maintains a deterministic relationship between velocity and density, using Gardner's law below the seafloor (Gardner *et al.* 1974).

3.1 Data pre-processing and derivation of the source wavelet

A mixture of four-component OBS and single-component OBH were utilized in this study; the FWI was performed on the hydrophone channel which was present for all instruments and yielded the highest signal-to-noise ratio. Spectral analysis of the hydrophone data showed that there is a reasonable signal-to-noise ratio at frequencies down to ∼3.0 Hz. As we wanted to match the modeled wavefield to the observed wavefield, without cycle skipping, we included signal at the lowest frequencies possible. A minimum phase Ormsby bandpass filter with corner frequencies of 2.0, 3.0, 4.5 and 6.5 Hz was applied to the hydrophone data in order to isolate the low-frequency signal from unwanted noise (Fig. 2a). Typical data pre-processing for the purpose of FWI may look to maintain the lower frequency data by simply applying a low-pass filter, but we needed also to diminish the effects of coherent low-frequency noise from the previous seismic shot. A top mute was applied ∼0.1 s before the first seismic arrival, in order to remove the noisy water column, and a bottom mute was applied 1.8 s after this top mute (Fig. 2b) in order to include the first-arriving wavefield which, at these frequencies, is about 1.0–1.5 s in length (Fig. 2a). This muting process creates a time window for the input field data which incorporates the direct water arrival and refractions through the crust (Pg) and upper mantle (Pn, Fig. 2b).

We use a free surface to represent the reflective sea surface, so, we use a deghosted source wavelet to generate synthetic data for FWI. The deghosted source wavelet is obtained using a Weiner matching filter and here, we used the following steps: (1) guessing a source wavelet by selecting a clear noise-free near-offset direct water-wave arrival into an OBS (OBS46 was selected), windowing this arrival by 1 s, and applying an identical bandpass filter to this guessed source wavelet and field data (Ormsby bandpass filter with corner frequencies of 2.0, 3.0, 4.5 and 6.5 H); (2) generating a synthetic water-wave arrival for the selected OBS using the guessed bandpass filtered source wavelet and starting model; (3) finding the inverse filter that matches this synthetic trace to the observed trace and (4) applying this inverse filter to the initial source guess to generate the new source wavelet. This new source was then used

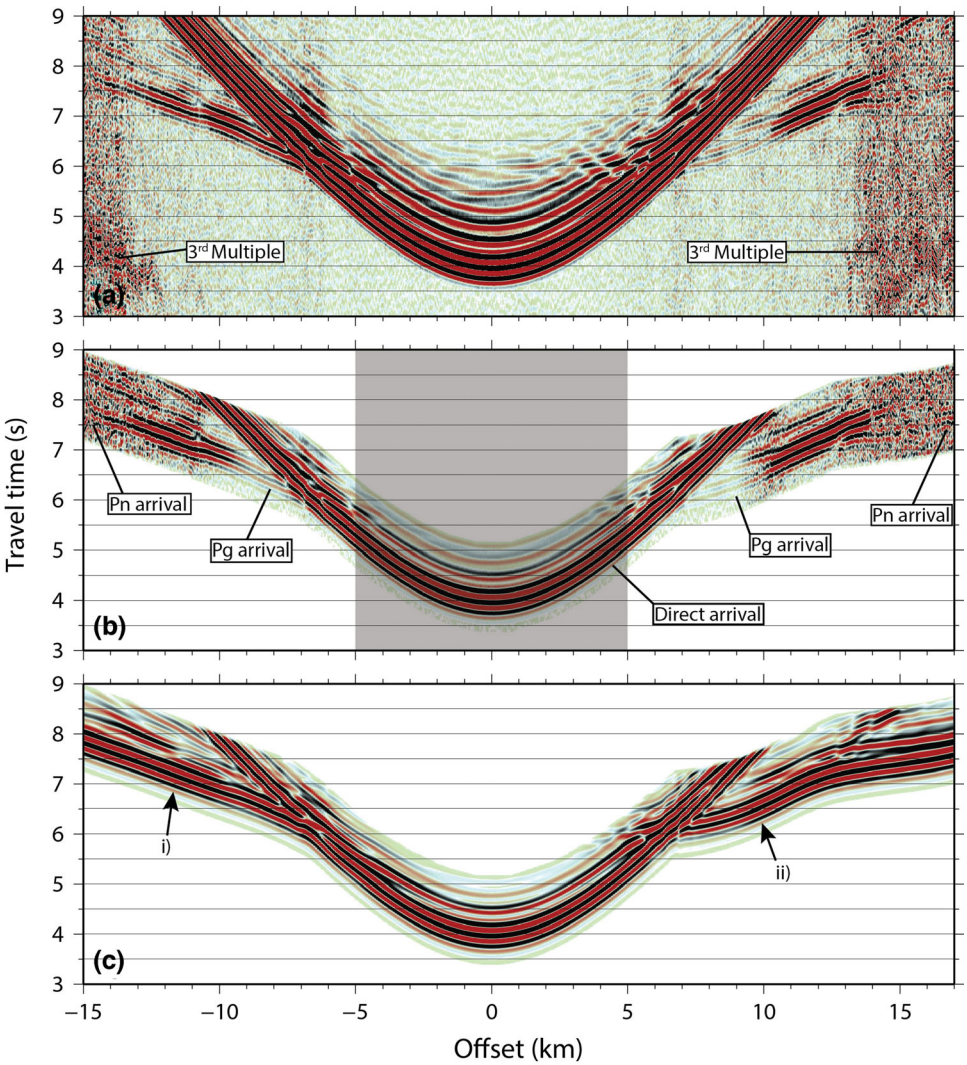

Figure 2. (a) Example receiver gather from OBS 46, filtered with an Ormsby bandpass comprised of corner frequencies 2–3 and 4.5–6.5 Hz. The third multiple from the previous seismic shot is indicated. (b) Same receiver gather as in (a), windowed 1.8 s after the first arrival for input into the inversion process. Grey area indicates data excluded from the inversion. Identified seismic phases are indicated. (c) Synthetic receiver gather for OBS46 generated using the starting velocity model in (a). Please note that receiver gathers, here and thereafter, are illustrated with a trace dependent gain for display purposes.

to generate the nearest offset direct wave through the water for all OBS and compared to the equivalent observed arrival (Fig. 3). The excellent match between the observed and synthetic data shows that this source wavelet is appropriate for all the OBS. The similarity of the waveforms for all OBS indicates that there is no significant change in the source wavelet during the survey, and that there are no significant differences in the OBS response at the frequencies used in the inversion.

3.2 Starting model

The starting model for the FWI process is a modified version of the 2-D compressional seismic traveltime tomography model described by Davy *et al.* (2016). This model was developed using OBS data collected from the Galicia-3-D seismic experiment, supplemented with data from the ISE-1 seismic profile (Sawyer *et al.* 1997; Zelt *et al.* 2003), and inverted using the 'TOMO2D' traveltime inversion code of Korenaga *et al.* (2000). The final TOMO2D model has an overall traveltime misfit of 53 ms, and a chi-squared value of 0.97. We shortened this model to include only the easternmost 68 km of the seismic profile where the OBS are more closely spaced, to a depth of 12 km, and defined the model on a grid with horizontal and vertical spacings of 50 m. FWI requires 4–5 model nodes per seismic wavelength (Warner *et al.* 2013), and so with water velocities of $\sim$1.5 km s^{-1} a node spacing of 50 m allows inversion frequencies of up to 6.0–7.5 Hz. In the TOMO2D analysis, a constant velocity of 1.52 km s^{-1} was used for the water column. This is sufficient for traveltime tomography, but not for reproducing consistently the first seismic arrivals to within half a cycle of those observed in the field data. Sound velocity profiles, used for the processing of the multibeam bathymetry collected during the survey, were used in place of this constant velocity approximation. The resulting model gives an accurate fit of the direct arriving waveforms through the water column (12.7 ms for all instruments, on average), as shown in Fig. 3.

Sediment velocities in this starting model were determined by the forward modeling of a prominent sedimentary reflector and very limited sediment refractions, and are therefore relatively unconstrained. This is the result of the large crossover distance between the direct water wave and the refracted arrivals from the subsurface,

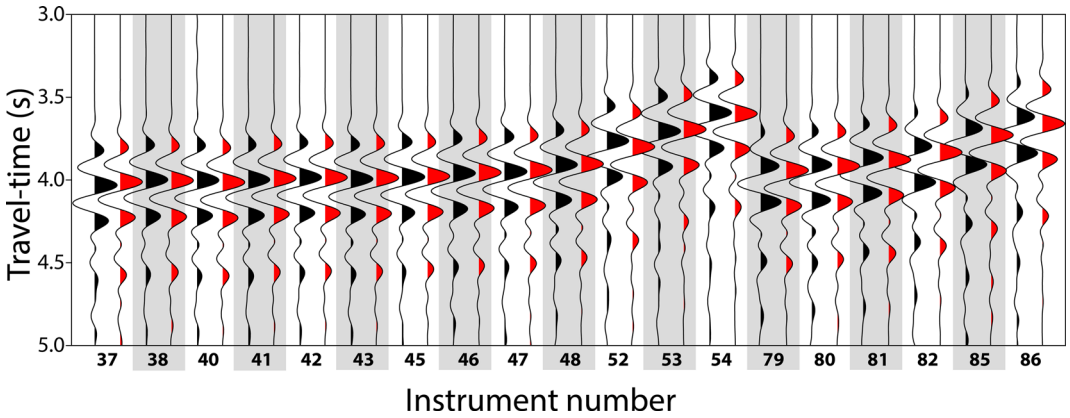

Figure 3. Fit between observed and synthetic direct water-wave arrivals. Observed near-offset traces (black) compared with the equivalent synthetic trace (red) through the starting velocity model, for all instruments used in this study. Observed data are bandpass filtered (Ormsby, corner frequencies 2–3 and 4.5–6.5 Hz).

dictated by the depth of the instrument deployment. The effect of uncertainty in sediment velocities on the final FWI velocity model is examined later in the paper.

The velocity model was smoothed in both the horizontal and vertical directions in order to remove any features that have a shorter wavelength than obtainable by FWI at the lowest inversion frequency. A 2-D convolution filter, using three samples in the vertical direction (150 m) and nine samples in the horizontal direction (450 m), was used for this smoothing process. Our starting model can be seen in Fig. 4(a).

3.3 Data selection

Using this starting velocity model, synthetic receiver gathers were produced with the same source–receiver geometry as the original seismic experiment (Fig. 2c). Synthetic gathers were used as a quality control for the field data to be input into the FWI process. Of the 20 instruments which yielded useable data, one was rejected for being too noisy. The final instrument coverage used for the FWI is shown in Fig. 1(b).

Within the offset range between 0 and 5000 m, the first arrivals comprise direct water waves and subhorizontally traveling turning waves which sparsely sample the shallow subseafloor (Fig. 2b). When included in the inversion these arrivals tend to dominate due to their large amplitudes, and the inversion attempts to match changes in waveform structure by introducing rapid changes in shallow subseafloor velocities which are poorly constrained. Pg and Pn arrivals travel subvertically through the shallow section below each OBS, and therefore pass relatively rapidly through this region, so their traveltimes will not be significantly affected by the shallow velocity structure. Thus, it was decided to exclude this offset range (0–5000 m) from the inversion, and not attempt to resolve velocity in the shallow subseafloor, which is a region of low scientific interest.

We assessed the data from each individual instrument to identify the maximum offsets to which the first seismic arrival could be positively identified and matched to the synthetic wavefields to within half a seismic cycle. Traveltime picks from Davy *et al.* (2016) were used as guidance in this process. These maximum offsets were then used as the upper bounds for data input for the respective instrument. Maximum input data offsets ranged from 13.0 to 23.0 km across the 19 instruments utilized in the inversion (Fig. 2b shows maximum data offsets used for OBS 46).

3.4 Inversion

We assumed an isotropic medium for the inversion, based on previous joint reflection and refraction traveltime tomography (Davy *et al.* 2016). These joint inversions resolved the *S*-reflector by constraining the velocity field using refraction data and determining the reflector depth using wide-angle reflections. These results showed an excellent match to the *S*-reflector resolved in reflection imaging, where ray paths are near vertical. This observation indicates that any anisotropy is quite weak, justifying our assumption of isotropy.

We developed the inversion by increasing progressively the cut-off frequency of the low-pass filter applied to the input data, which was set at 3.0, 3.4, 3.9, 4.5 and 5.2 Hz (Fig. 4). Velocities of below 2.0 km s^{-1} in the starting model were kept constant during the inversion to keep the water velocity and sea bottom fixed, since these parameters had been determined independently, and were confirmed by synthetic direct water waves through the starting model (Fig. 3). Velocities were not allowed to be updated above 8.50 km s^{-1} as this was considered to be the maximum realistic value for the uppermost mantle here. The inversion process was iterated 10 times for each filter setting, with the resulting velocity model acting as the input to the next inversion iteration (Fig. 4). After 10 inversion iterations at each bandwidth, the reduction in the model misfit was less than 0.5 per cent of the previous inversion iteration, which we believed to be a sufficient convergence (Fig. 5). Relatively small reductions in the misfit functional were seen for each inversion frequency, see Table 1.

The complete inversion process runs through 50 iterations to produce the final inversion model (Fig. 4f). Systematically introducing higher frequencies of input data into the inversion process gradually increases the resolution of the resulting velocity model (Figs 4a–f).

Testing of the inversion parameters included examining the effects of: the maximum data offsets used, the length of the time window around the first seismic arrival, and uncertainty in the sediment velocities in the starting model. The results of these parameter tests were checked against reflection seismic images, and the observed field data, in order to make informed decisions on the best parametrization. The next three subsections describe the results of these tests.

3.5 Data offsets

One of the limitations of this data set is the range of useable data offsets. Given the deep-water setting, Pg refractions only become first

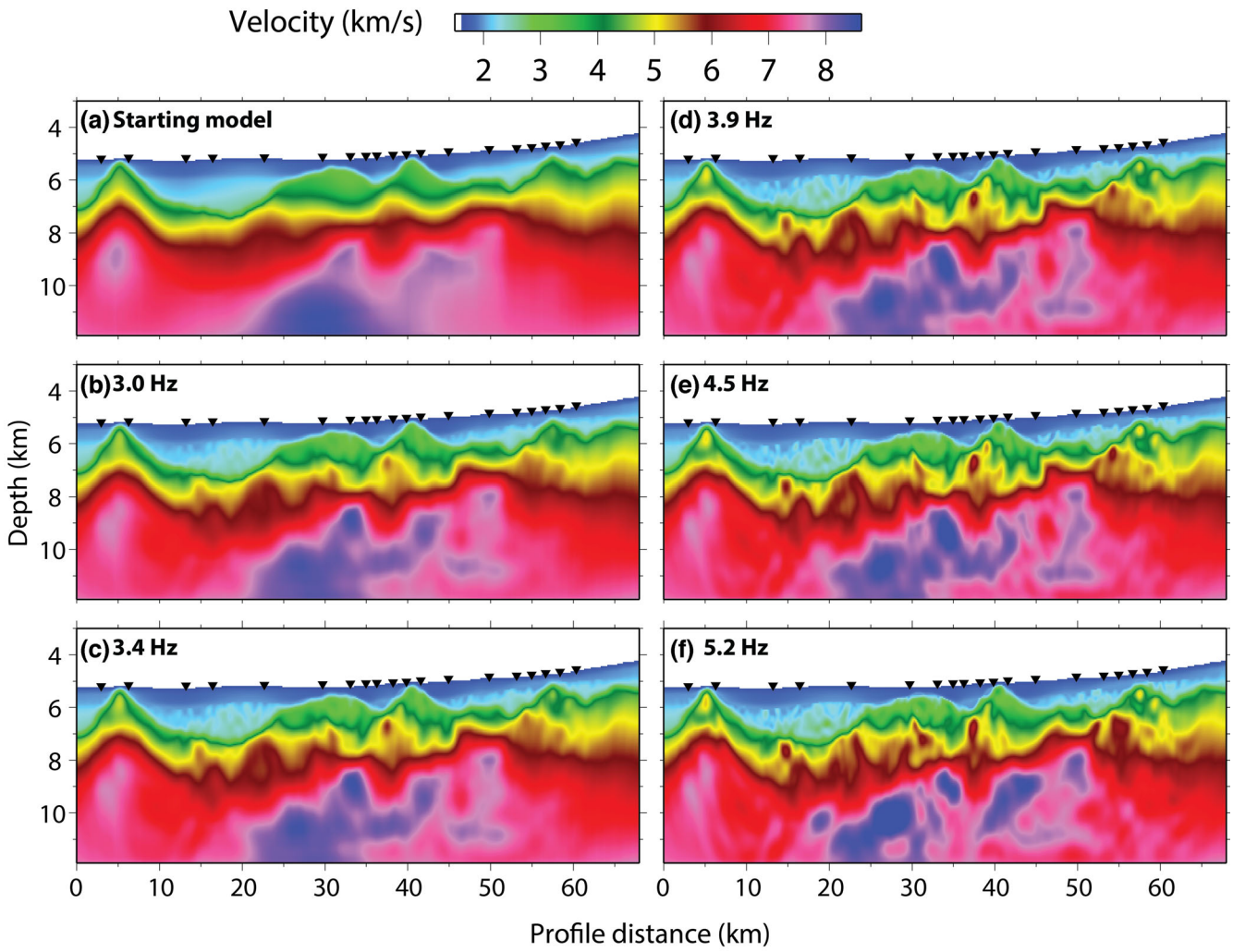

Figure 4. (a) Starting velocity model input to the FWI. Results of the iterative FWI process for low-pass filter frequencies of: (b) 3.0 Hz; (c) 3.4 Hz; (d) 3.9 Hz; (e) 4.5 Hz and (f) 5.2 Hz. Black upturned triangles indicate the locations of utilized instruments. Vertical exaggeration is 3.2.

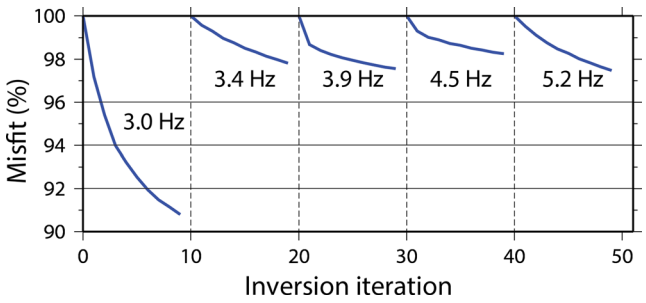

Figure 5. Misfit reduction versus inversion iterations for the five low-cut frequency bands, 3.0, 3.4, 3.9, 4.5 and 5.2 Hz.

Table 1. Reduction in misfit functional for given inversion low-pass frequencies. Each frequency is iterated 10 times.

Inversion low-pass frequency (Hz)	Reduction in misfit functional (per cent)
3.0	9.2
3.4	2.2
3.9	2.4
4.5	1.8
5.2	2.5

arrivals at offsets of >5000 m, reducing our ability to resolve shallow subsurface structure. At longer offsets (> ∼12 000 m), the data become adversely affected by coherent noise from the third multiple (and higher order multiples) of the previous seismic shots (Fig. 2a). This is problematic because the crustal targets (fault rotated continental blocks, the *S*-reflector and uppermost mantle) are up to 5000 m below the seafloor, but we can only expect to resolve targets at depths approximately between a sixth and third of the maximum source–receiver offset (Warner *et al.* 2010; Morgan *et al.* 2013). This means that our inversion model, for data offsets >12 000 m, may be prone to noise-induced artefacts when attempting to resolve structure at depths greater than 2000–4000 m below the seafloor. To test whether our selected maximum data offsets (between 13.0 and 23.0 km) produced a robust model, we tested arbitrary maximum data offsets of 10, 15 and 20 km for all instruments used in the inversion. All other inversion parameters were identical to those described in Section 3.4. Fig. 6 shows the resulting models and 1-D profiles at set distances through each model.

When limiting input data offsets to 10 km (Fig. 6a), the resulting velocity model has many closed velocity contours, high lateral and

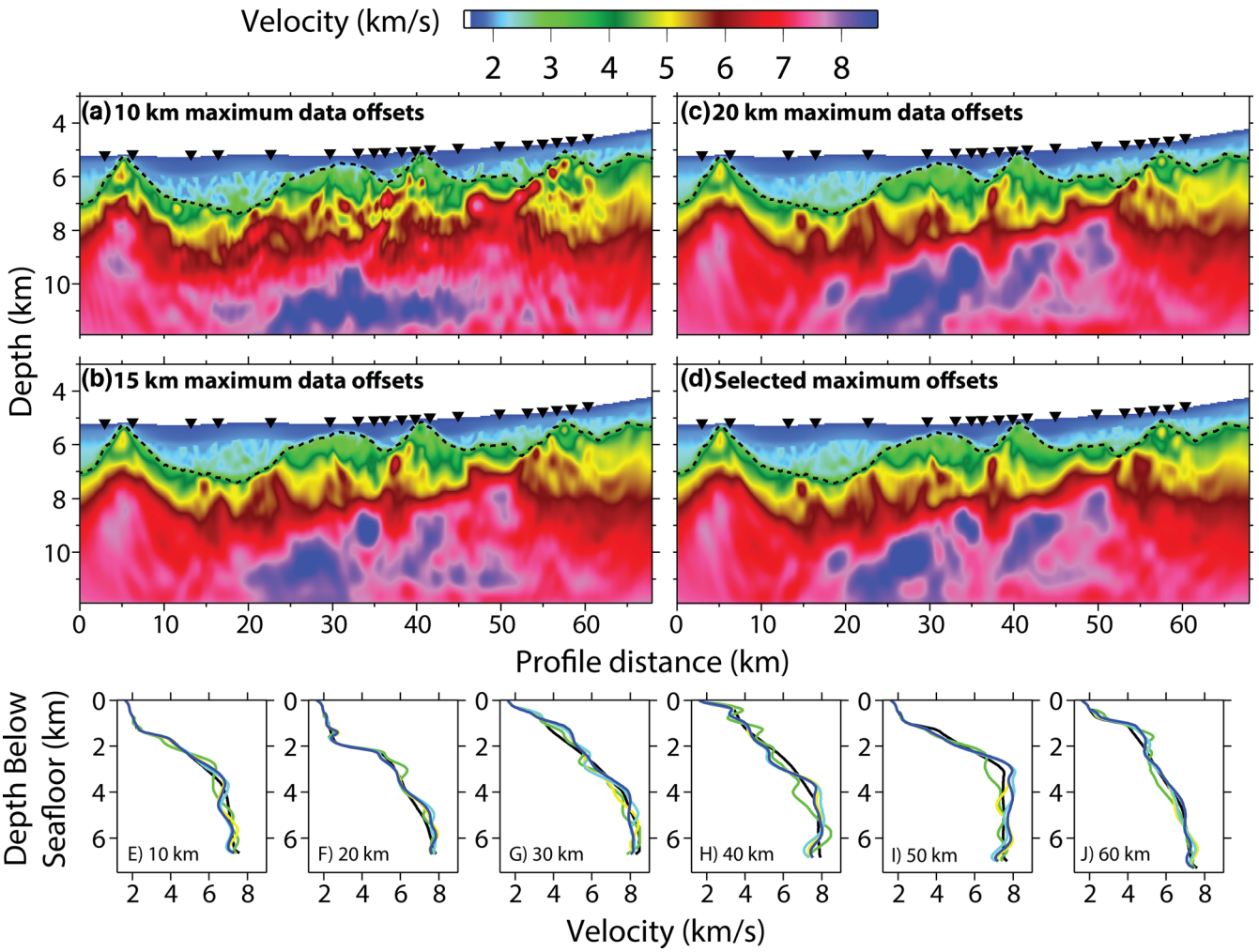

Figure 6. Inversion models for maximum data offsets of (a) 10 km, (b) 15 km, (c) 20 km and (d) instrument specific offsets. Black upturned triangles indicate the locations of utilized instruments and black dashed line indicates the base of post-rift sediments. Vertical exaggeration is 3.2. (e)–(j) 1-D velocity profiles through the resulting models, below the seafloor, at set profile distances (10, 20, 30, 40, 50 and 60 km, respectively). Line colours are black: starting model, green: 10 km data offsets, yellow: 15 km data offsets, light blue: 20 km data offsets and blue: instrument specific data offsets.

depth variability, and features which would be described as non-geological. This is expected given the sparse coverage and relatively shallow depth of penetration when offsets are limited to 5–10 km, as waves are expected to only travel to depths of 1.6–3.3 km below the seafloor. It can be seen in the 1-D plots (Figs 6e–j) that the model utilizing 10 km data offsets has a good correlation with the trends of the other models to depths of ∼ 1.2–3.0 km below the seafloor, as would be expected. The only exception to this is at ∼40 km profile distance (Fig. 6h). Below these depths, the 10 km offset model varies from the other models by up to 1.38 km s^{-1} (e.g. 3.0 km below the seafloor at 50 km profile distance), because the model is unconstrained at these depths.

The remaining three models share common features and velocity values. These models appear much smoother than that produced using data offsets from 5 to 10 km. The 1-D velocity profiles confirm that the models have common trends with depth, throughout the model (Figs 6e–j), but we observe that the model utilizing offsets of 15 km deviates from our final inversion model and that using maximum offsets of 20 km, at depths greater than 4 km below the seafloor on profiles at 10, 30 and 50 km. Again, these deviations are unsurprising given that the expected depth of penetration when using maximum offsets of 15 km is up to 2.5–5.0 km.

This similarity, especially between models using 15 and 20 km offset of input data, indicates that incorporating data with coherent noise yields results which are comparable to those inversions which exclude noisy data altogether. These results also suggest that the FWI is relatively insensitive to noise.

3.6 Data windowing

Data input into the inversion process were top and bottom muted, allowing a 1.8 s window of data to be matched in the inversion process. This time window was determined heuristically in order to include only the primary compressional seismic phase arrivals (i.e. Pg and Pn, Fig. 2a), while excluding mode-converted later arrivals, which cannot be reproduced by the acoustic wave approximation (Jaiswal *et al.* 2008).

Windows of 1.8 s were selected, based on inspection of the length of the bandpassed first-arriving waveform (Fig. 2a). To investigate the effect of the data window length, the inversion process was run also with data windows of lengths 1.0, 1.5, 2.0 and 2.5 s (Fig. 7). It appears that longer window lengths introduced more complicated structure to the resulting velocity model, a result of the inversion process trying to fit the later parts of the seismic coda and later

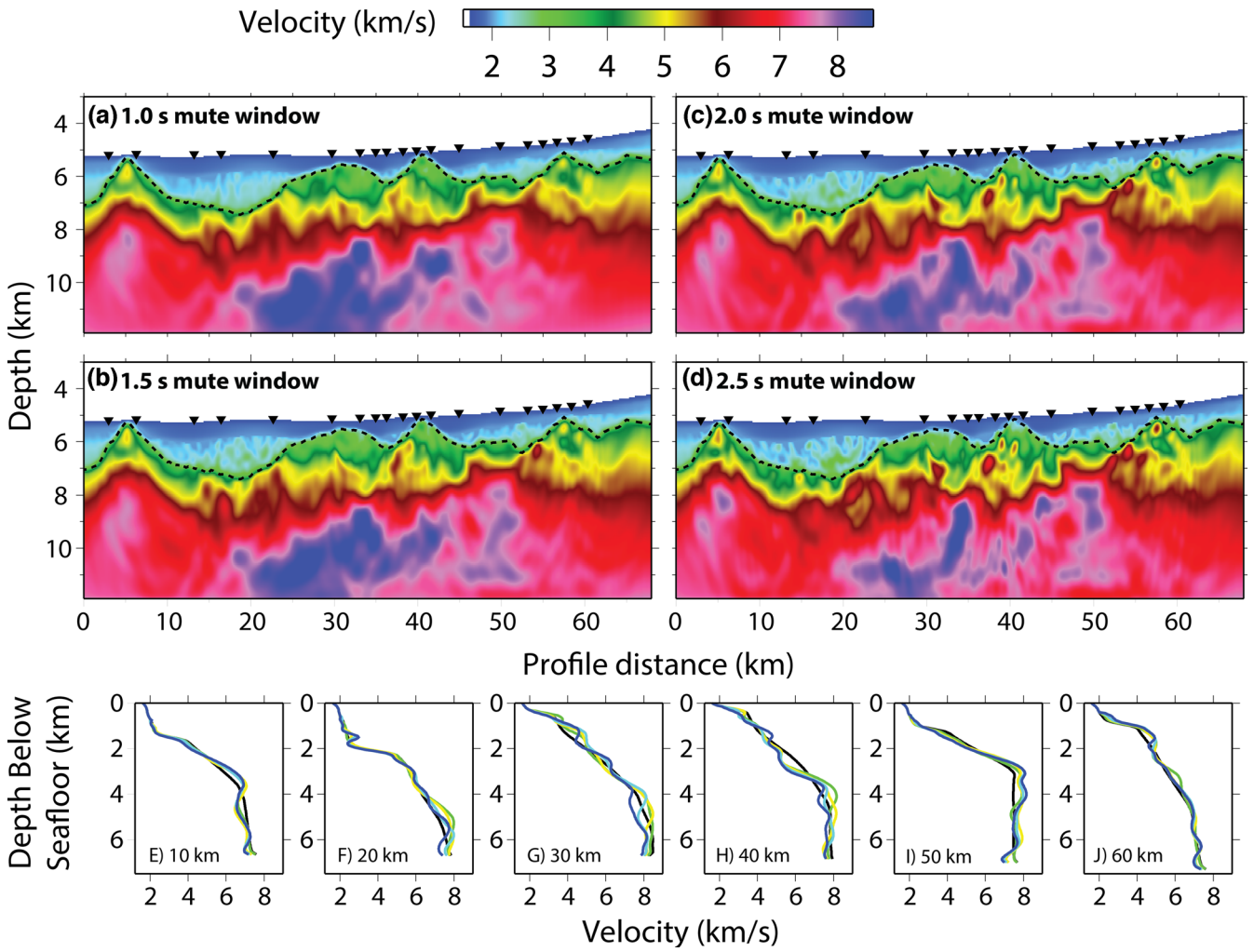

Figure 7. Inversion models for varying mute windows of (a) 1.0 s, (b) 1.5 s, (c) 2.0 s, (d) 2.5 s. Black upturned triangles indicate the locations of utilized instruments and black dashed line indicates the base of post-rift sediments. Vertical exaggeration is 3.2. (e)–(j) 1-D velocity profiles through the resulting models, below the seafloor, at set profile distances (10, 20, 30, 40, 50 and 60 km, respectively). Line colours are black: starting model, green: 1.0 s, yellow: 1.5 s, light blue: 2.0 s and blue: 2.5 s.

arrivals. A time window of 2.5 s resulted in a rough model with a significant number of closed velocity contours, which are geologically unlikely for this setting. Conversely, a time window of 1.0 s resulted in a smooth model, which is geologically reasonable, but failed to match reflections in the seismic images as well as inversion model using a time window of 1.8 s. We also observed a significant decrease in seismic velocity in the resolved upper mantle in the central section of the profile, with an increasing window length (depths of 9.0–10.5, 25.0–32.0 km profile distance, Figs 7c and d; deeper than 4.0 km below seafloor in Fig. 7g). Despite these differences, the overall velocity structure observed in the plots and the trends of the 1-D velocity profiles, remained relatively constant. Consistency in the resulting FWI models and the observed depth–velocity profiles, when using time windows of 1.0, 1.5 and 2.0 s for FWI, indicates that our chosen time window of 1.8 s is appropriate.

3.7 Sedimentary velocities

As mentioned earlier in this section, the post-rift sediment velocities in the starting model were poorly constrained, so we test the effects of varying post-rift sedimentary velocities in the starting model. In the original model, the post-rift sediments were defined by two discrete sedimentary layers; the top has velocities increasing from 2.00 to 2.15 km s^{-1}, while the bottom layer has velocities increasing from 2.30 to 2.60 km s^{-1}. These layers were constrained by intersedimentary reflectors (at offsets <5000 m) and limited sedimentary refractions (at offsets >5000 m). To test the uncertainty in sedimentary velocities in our starting model, we performed the TOMO2D traveltime inversion of Davy *et al.* (2016) with starting models possessing low sediment velocities (1.80–2.00 km s^{-1}), high sediment velocities (2.60–3.00 km s^{-1}), a low–velocity gradient (2.30–2.50 km s^{-1}) and a high-velocity gradient (1.80–3.20 km s^{-1}). All traveltime inversion parameters remained identical to that described in Davy *et al.* (2016). The outputs of these traveltime inversions were then used as the starting models for the FWI process, with the inversion results observable in Fig. 8. With the exception of the low sediment velocity model, the general velocity structure below the post-rift sediments remains consistent. Where post-rift sediment velocities are low, higher velocities are observed directly below the top of the syn-rift sediments, and vice versa where the post-rift sediment velocities are high. This behaviour is a result of both the traveltime tomography and FWI. The phenomenon is amplified in areas of thicker post-rift sediment (i.e. at 10, 20 and 50 km profile distance). For example, at 50 km profile distance the

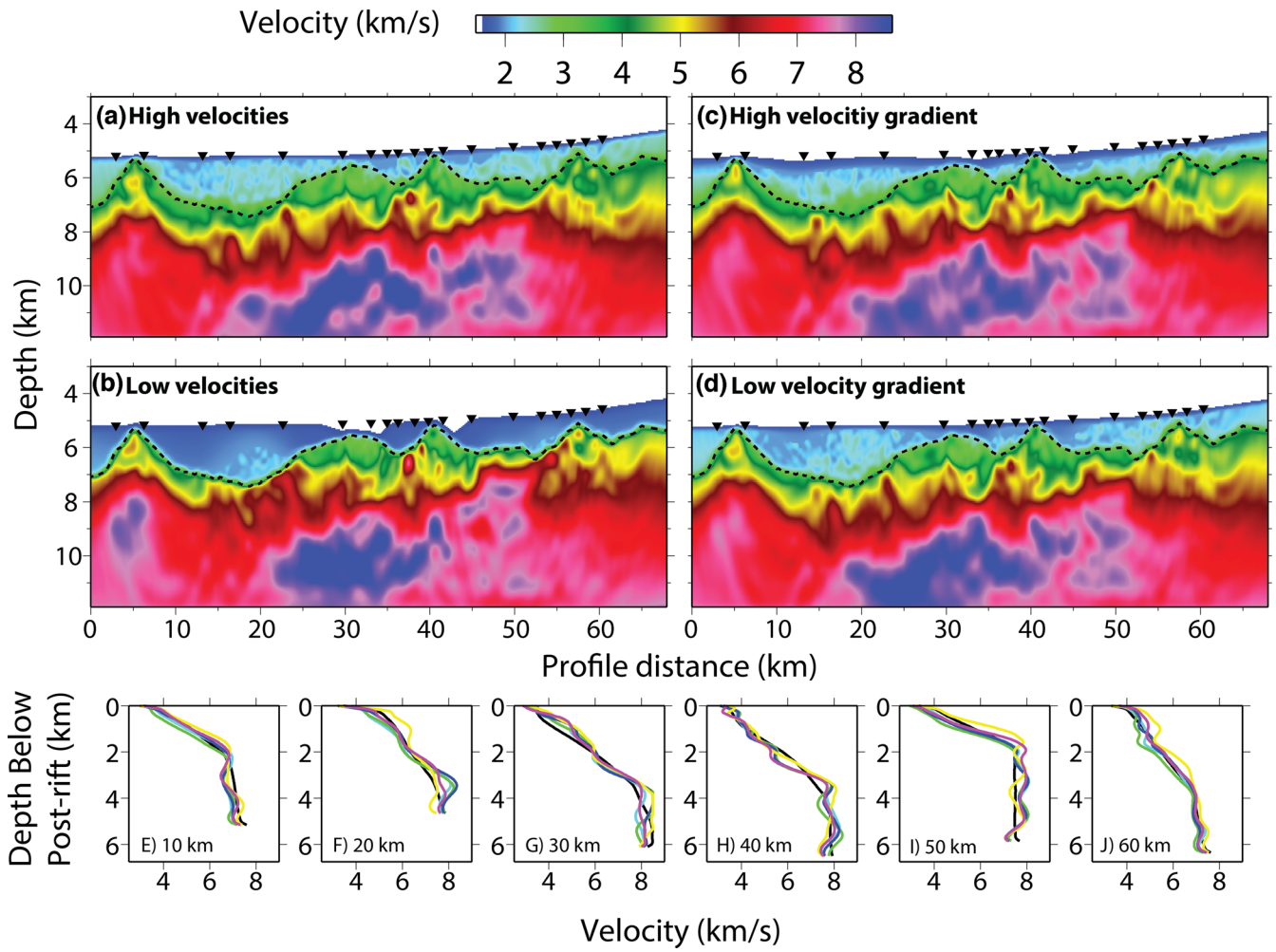

Figure 8. Inversion models for varying starting sediment velocity models, as described in Section 3.7: (a) high velocities, (b) low velocities, (c) high-velocity gradient and (d) Low-velocity gradient. Black upturned triangles indicate the locations of utilized instruments and black dashed line indicates the base of post-rift sediments. Vertical exaggeration is 3.2. (e)–(j) 1-D velocity profiles through the resulting models, below post-rift sediment, at set profile distances (10, 20, 30, 40, 50 and 60 km, respectively). Line colours are black: starting model, green: high velocities, yellow: low velocities, light blue: high-velocity gradient and blue: low-velocity gradient.

difference between the low and high sediment velocity models is 1.75 km s^{-1} at 1.65 km below the base of the post-rift sediment (Fig. 8i). This result indicates that variations in the starting post-rift sedimentary velocities are compensated for by the velocities below the post-rift sediment, in order for the total traveltimes to fit. Along the representative depth–velocity profiles (i.e. 10, 20, 30, 40, 50 and 60 km profile distance), the depth-averaged range of velocities recovered for the range of starting models, excluding the low-velocity post-rift sediment velocity model, is 0.12 km s^{-1}. We conclude that, since the sediments are unlikely to have such low velocities, the overall velocity structure of the inversion models below the post-rift sediment are minimally affected by uncertainty in the post-rift sedimentary velocities.

3.8 Assessing the modeled wavefield

One measure of the success of FWI is how accurately the observed wavefield is reproduced, and this is done by comparison with the synthetic wavefield. Fig. 9 shows the propagation of the source wavelet through the final inversion model to produce the synthetic wavefield. In this example, we have reversed the source and receiver configuration and are treating the OBS 46 as the seismic source, and the shot locations as receivers. This approach demonstrates the interaction of the wavefield with subsurface structure, and how that results in the observed wavefield. East of OBS 46, the wavefield refracts through significant subsurface topography in the form of a rotated continental fault block, giving the traveltime of the first seismic arrival significant lateral variability (arrow ii, Fig. 2c). Conversely, west of OBS 46, the top of the rotated continental fault block dips smoothly westward, resulting in a first seismic arrival of little variation (arrow i, Fig. 2c). These synthetically produced traveltime features, resulting from the modeled subsurface topography, match those in the observed wavefield (Figs 2a and b).

In order to compare the match between the observed and modeled wavefields, we interleaved traces from alternative offset bins of 200 m (i.e. traces with instrument offsets between 200–400, 600–800 m, etc. are taken from the observed wavefield and are combined with traces with instrument offsets between 0–200, 400–600 m, etc. from the synthetic wavefield; Figs 10–12a and b). Where the wavefields match, a continuous wavefield will be observed over distances greater than the 200 m trace bins. Where the match is poor, a discontinuous wavefield will be observed over such distances. Comparing the observed wavefield with the synthetic wavefield

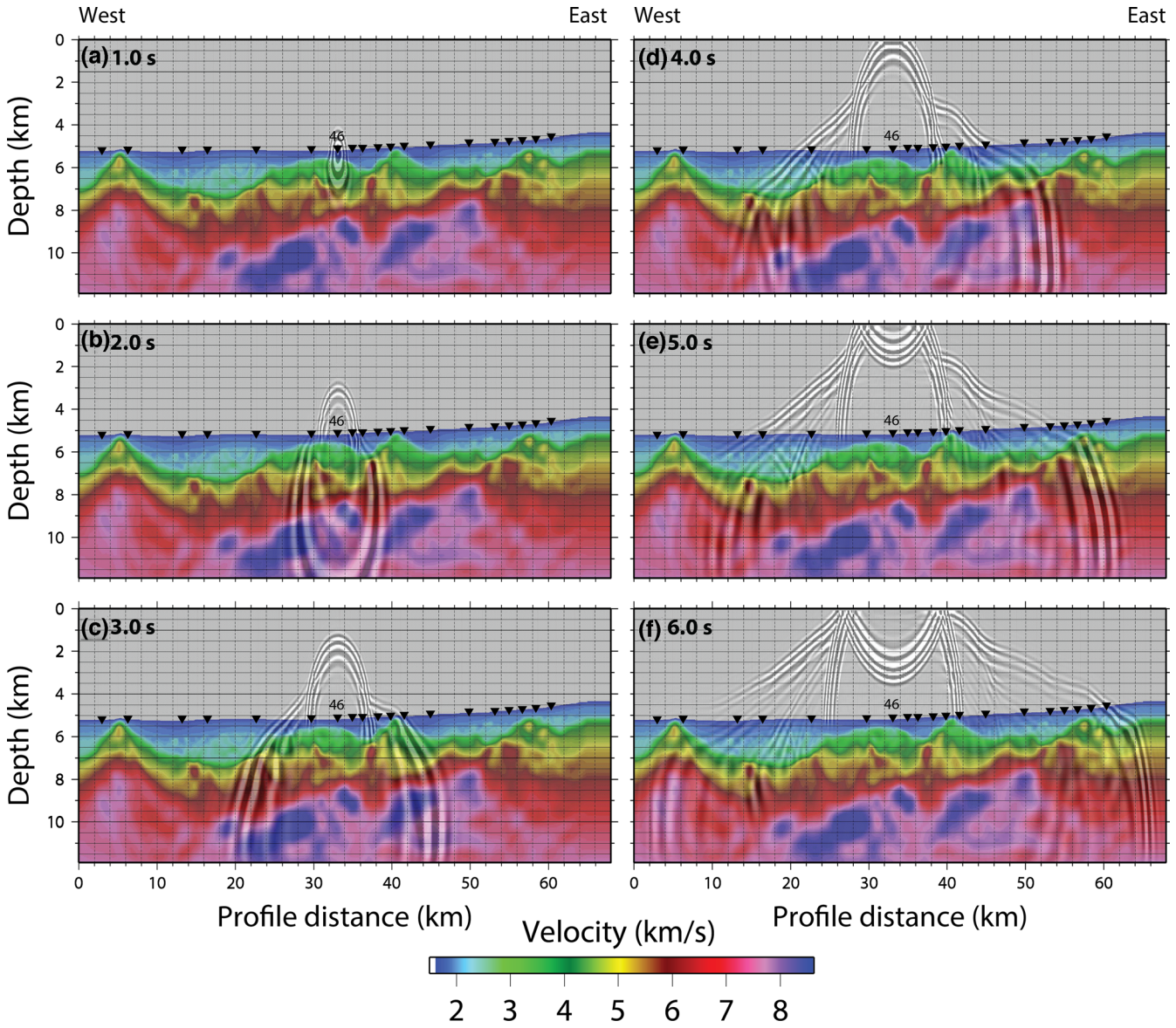

Figure 9. Propagation of the derived source wavelet through the final inversion model, originating at OBS46, at discrete times: (a) 1.0 s, (b) 2.0 s, (c) 3.0 s, (d) 4.0 s, (e) 5.0 s and (f) 6.0 s. Black upturned triangles indicate the locations of utilized instruments. Vertical exaggeration is 3.2.

through the starting model (Figs 10–12a), it can be seen that the direct water arrival (-7.0–7.0 km) shows high continuity, indicating that the starting velocity model has reasonably accurate water and subseafloor velocities. The wavefield appears to be fairly consistent at some wider offsets, for example between −11 and −15 km on OBS 46 (Fig. 11a) and −10 and −14 on OBS 54 (Fig. 12a), indicating that the starting model at depth is close to the true velocity structure in particular areas. There are also notable mismatches in the first seismic arrivals, outside the direct water arrival, for example at offsets between −7 and −11 km and between 7 and 13 km on OBS 46 (Fig. 11a) and 6–10 km on OBS 37 (Fig. 10a), which indicates that the velocities in sections of the thinned continental crust are not reproducing the wavefield accurately. However, these mismatches appear to be less than half a seismic cycle, which is a pre-requisite to avoid cycle skipping during the FWI process. Significant improvements in the match between wavefields are observed when comparing the observed and synthetic wavefield through the FWI velocity model (Figs 10–12b). Areas previously mismatched (e.g. between offsets of 7–13 km on OBS 46) now appear more continuous (see arrows) indicating that the FWI process has modified the subsurface velocities in such a way that the traveltime and phase of these synthetic waveforms match those that are observed. Where the starting model already matched the observed wavefield well there is little to no change, as would be expected.

Directly comparing traces at set offsets also shows how the synthetic waveforms are modified through the FWI process. Figs 10(c)–(h), 11(c) –(g) and 12(c) –(g), show trace-to-trace comparisons of the observed and synthetic wavefields through the starting velocity model, while Figs 10(i)–(n), 11(h)–(l) and 12(h)–(l), show trace-to-trace comparisons of the observed and synthetic wavefields through the final velocity model. Despite the small changes in the inversion misfit (Fig. 5), we observe significant improvements in the synthetic wavefield. For example, at offsets of −10.05, −7.52, 8.63 and 11.93 km on OBS 46 (Figs 10d-g), the synthetic traces through the starting model exhibit shapes close to the observed waveform, but with amplitude differences and phase shifts within half a seismic

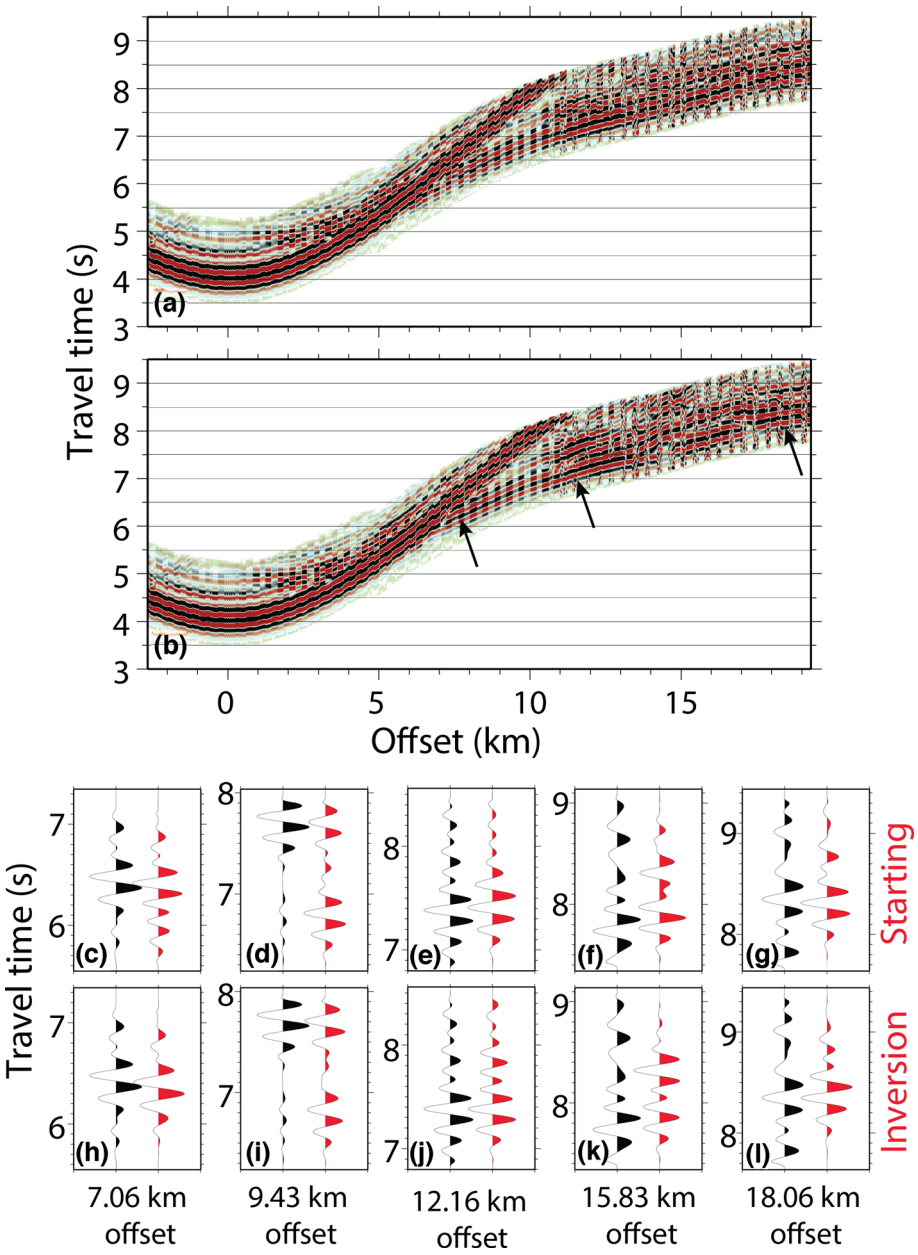

Figure 10. OBS 37. (a) Observed data interleaved with synthetic through the starting model in alternative offset bins of 200 m. (b) Observed data interleaved with synthetic through the inversion model in alternative offset bins of 200 m. (c)–(g) Black traces: observed data and red traces: synthetic data through the starting model. (h)–(l) Black traces: observed data and red traces: synthetic data through the FWI model.

cycle. After the FWI, the synthetic traces have relative amplitudes and phases that match well the observed traces (Figs 10j−m), indicating that the new velocity model is a more accurate representation of the subsurface. Observed traces at the furthest input offsets (i.e. −14.92 and 16.80 km on OBS 46, 18.06 km on OBS 37 and −17.57 km on OBS54, Figs 11i and n, 10l and 12h, respectively) are being affected by coherent noise, and FWI is struggling to match these more complicated waveforms. It appears that the trace at −14.92 km on OBS 46 is cycle skipped in the starting model, and although the inversion has led to an improvement in the shape of the waveform it has not changed its traveltime, which should be earlier. The onset of reduced performance of FWI at longer offsets reinforces the decision to limit the offsets of the input data, based on visual inspection of the match between the observed data and synthetic data from the starting model.

3.9 Checkerboards

The maximum achievable resolution of the final FWI velocity model was assessed by a series of checkerboard tests (Zelt & Barton 1998). Alternating velocity perturbations of ± 2 per cent were introduced into the starting velocity model in checkerboard patterns to create reference models with anomaly dimensions of 10.0 km × 2.0 km, 5.0 km × 1.0 km and 2.5 km × 0.5 km (Fig. 13). Small velocity perturbations of ± 2 per cent are used in order to avoid major changes in the modeled wave paths, which could lead to the synthetic data generated from the checkerboard and starting model being cycle skipped. Synthetic receiver gathers were then produced through these reference models by forward modeling of the wavefield, using the same shot-receiver geometry as the receiver gathers used in the FWI. These synthetic receiver gathers were windowed and

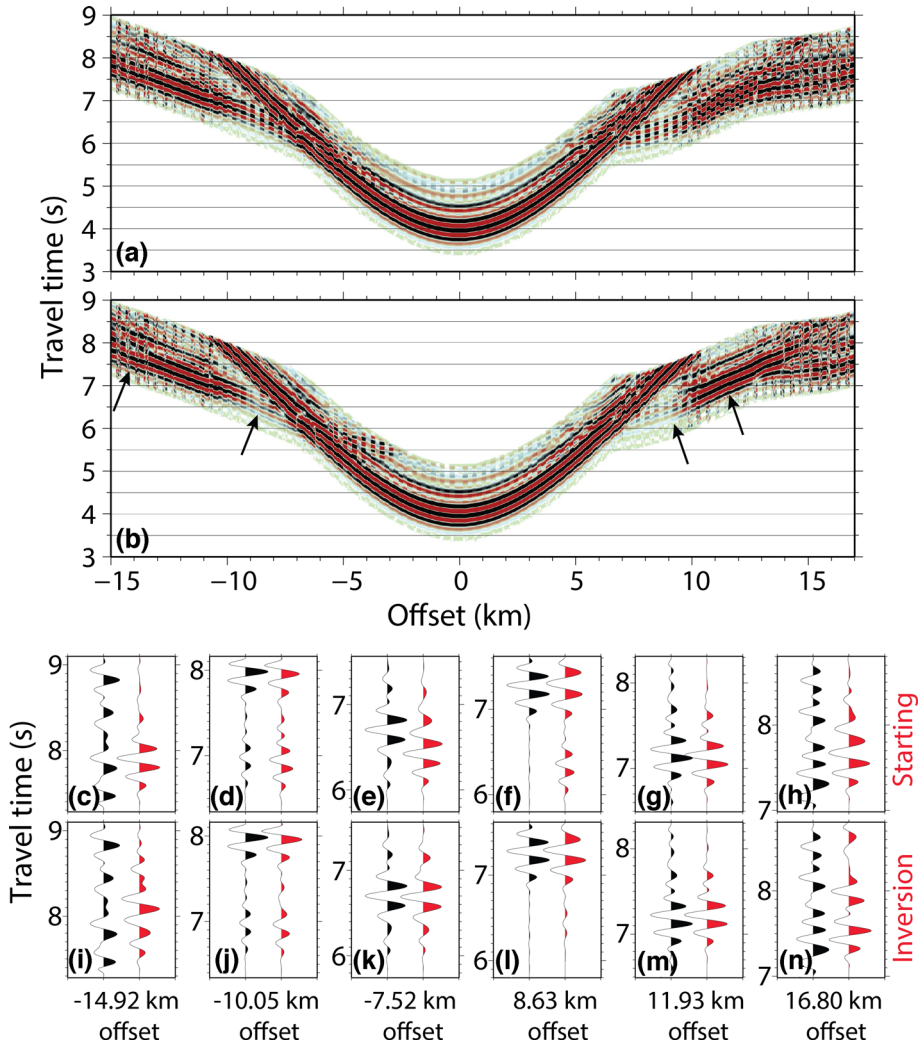

Figure 11. OBS 46. (a) Observed data interleaved with synthetic through the starting model in alternative offset bins of 200 m. (b) Observed data interleaved with synthetic through the inversion model in alternative offset bins of 200 m. (c)–(h) Black traces: observed data and red traces: synthetic data through the starting model. (i)–(n) Black traces: observed data and red traces: synthetic data through the FWI model.

inverted with identical FWI parameters. The differences between these inversion results and the unperturbed starting velocity model were used to determine the length scale of structure resolvable in the final FWI model (Fig. 13).

There is an observable diagonal smearing of the resolved checkerboard patterns at the eastern and western limits of the model, for all scales of velocity perturbation. This phenomenon occurs between checks of equal polarity, at profile distances <10 and >50 km. This smearing is likely to be the result of the subsurface being sampled by unidirectional wave propagation and limited data offsets in these areas of the model.

Large-scale structure (10.0 km $\times$ 2.0 km) is very well resolved throughout the central portion of the model, but exhibits a small deterioration in the recovered anomaly amplitudes below 10 km depth. Medium-scale structure (5.0 km $\times$ 1.0 km) is still well resolved, but starts to exhibit slight smearing between checks where there is lower instrument coverage (e.g. 5.0–30.0 km profile distance), and again at depths >10 km. Fine-scale structure (2.5 km $\times$ 0.5 km) is the least well resolved, as is to be expected, but much of the structure at this scale is still recoverable throughout the model. Fine-scale structure is particularly well resolved between profile distances of 30.0–42.0 and 52.0–60.0 km, where the coverage of instruments is densest. Other regions of the model start to reveal a greater degree of smearing between checks, primarily between diagonally linked checks.

The results of these resolution tests exhibit a significant improvement over the minimum resolution of approximately 5.0 $\times$ 2.5 km, achieved in the traveltime tomography of Davy *et al.* (2016). However, it should be noted that these resolution tests are done with synthetically produced wavefields and thus represent the maximum achievable resolution with the given experimental geometry.

4 RESULTS AND DISCUSSION

The final FWI velocity model in depth can be seen in Figs 4(f) and 6(d). Overall, the long-wavelength velocity structure remains consistent with that of the starting traveltime tomography model. Within the velocity model, we observe well-defined rotated continental fault blocks which overlie the *S*-reflector, and the Peridotite Ridge in the west. The FWI result reveals features in the velocity model with shorter wavelengths and a greater lateral variability to those that are observed in the starting model, indicating an increase in the resolution of the velocity structure along this seismic line.

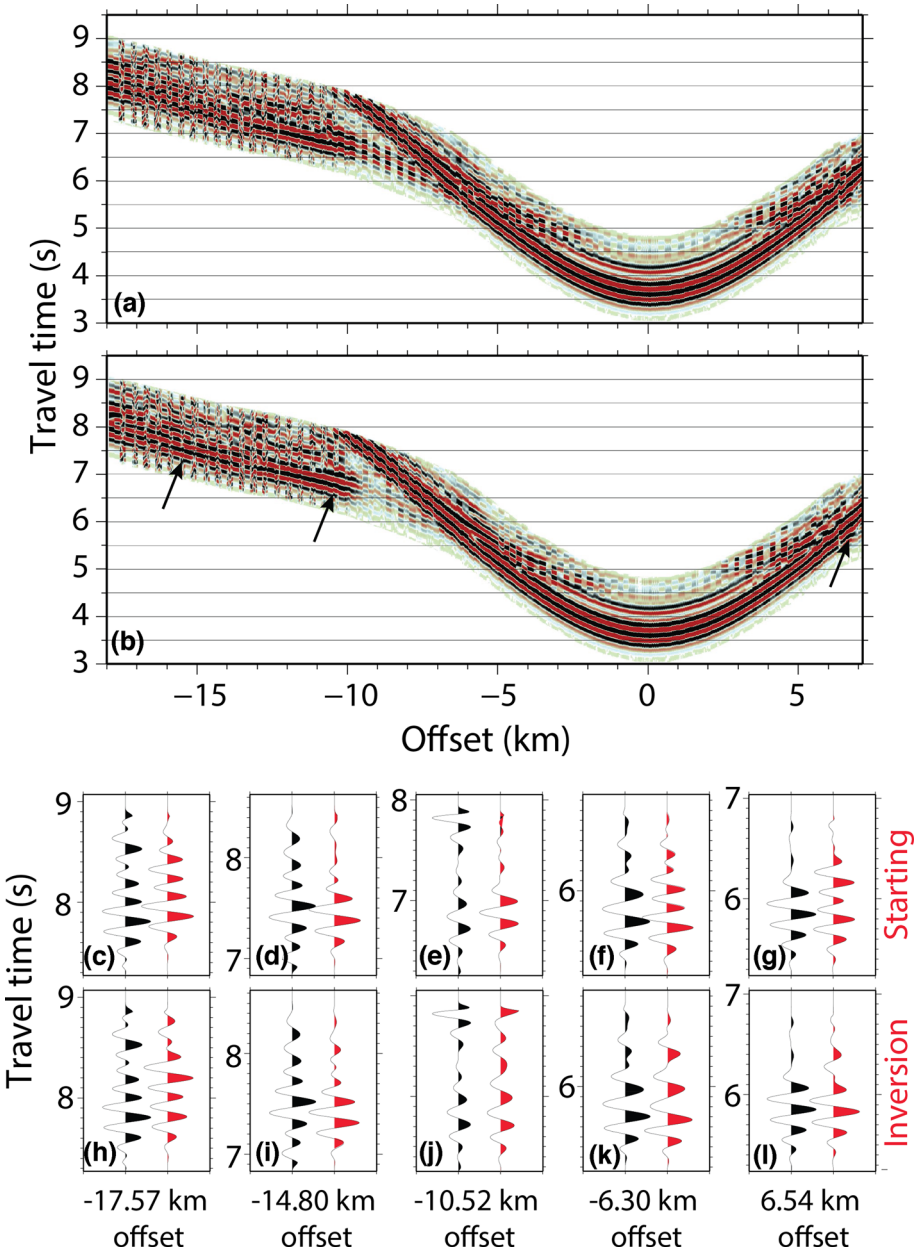

Figure 12. OBS 54. (a) Observed data interleaved with synthetic through the starting model in alternative offset bins of 200 m. (b) Observed data interleaved with synthetic through the inversion model in alternative offset bins of 200 m. (c)–(g) Black traces: observed data and red traces: synthetic data through the starting model. (h)–(l) Black traces: observed data and red traces: synthetic data through the FWI model.

4.1 Comparison with seismic images and interpretations

In order to assess whether the FWI has resolved the velocities of fine-scale subsurface structure, we compare the final velocity model with the structure observed in reflection seismic imaging. To make this comparison, we have utilized existing high-resolution 3-D multichannel reflection seismic images, which have been processed through to 3-D pre-stack Kirchhoff time migration. This reflection imaging was produced using the full 3-D seismic volume, which has a wide azimuth of shots and receivers, and yields a high-fidelity image of the subsurface. We converted our final FWI velocity model to time, and overlaid it onto the time migrated reflection image of seismic inline 420 (Figs 14 and 15). Additionally, we have overlain the interpretation of significant and relevant faults and geological horizons. Significant horizon reflections are seen from the base of the post-rift sediment, a strong intra syn-rift reflector, the top of crystalline basement, and the *S*-reflector. These interpretations have been made consistently throughout the 3-D seismic volume and are independent from both our starting and FWI velocity models. For the prominent normal faults and continental blocks observed through this section, we have adopted the naming convention of F3–F8 and B3–B7, respectively (Borgmeyer 2010; Ranero & Pérez-Gussinyé 2010).

4.1.1 Long-wavelength structure

Long-wavelength features that were already present in the starting velocity model show a strong correlation with the large-scale features imaged in the reflection seismic, such as the Peridotite Ridge,

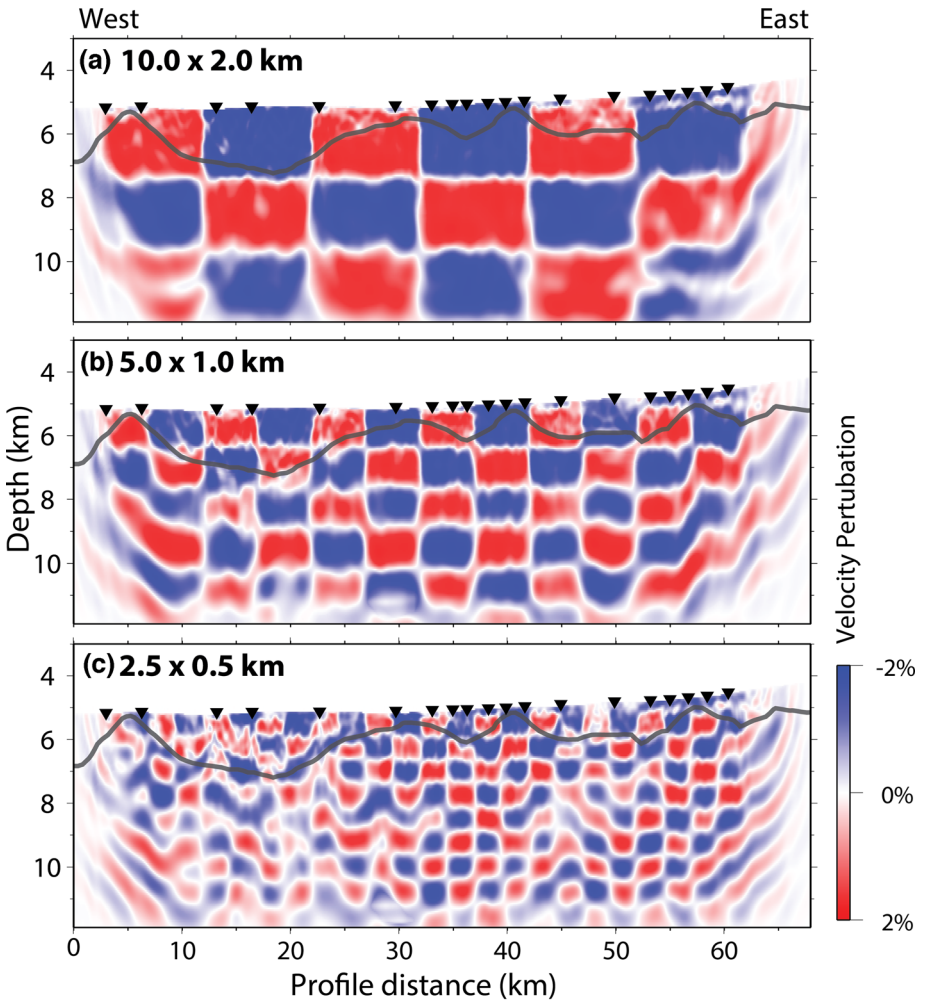

Figure 13. Checkerboard resolution test results. Anomaly check dimensions: (a) 10.0 × 2.0 km, (b) 5.0 × 1.0 km and (c) 2.0 × 0.5 km. Vertical exaggeration is 3.4. Grey line represents the top of the syn-rift sediments.

the major fault-rotated continental blocks (e.g. B3–B6) and the *S*-reflector detachment surface (Fig. 14d, Davy *et al.* 2016). These features retain their long-wavelength velocity structure through the FWI process, and shorter wavelength velocity features are revealed within the previously resolved features. The most apparent and significant changes to the velocity model occur in continental fault blocks B4–B7 within the pre-/syn-rift sediments and the top of crystalline basement. Areas of particular interest are identified by dashed boxes in Fig. 14 and are shown at a larger scale in Fig. 15. Features within these areas are discussed in detail in the next subsection. Outside of these regions, we observed notable features at both the western and eastern limits of the inversion model.

There is a deepening of seismic velocities between 6.0 and 7.0 km s^{-1} on the eastern flank of the Peridotite Ridge (7.0–12.0 km profile distance, arrow i, Fig. 14e). This deepening could indicate that the serpentinization of the mantle peridotite in this area is more pervasive than previous models have indicated. This area of decreased seismic velocities is coincident with the interpreted western limit of the *S*-reflector and the suggested location of normal fault F8, which could have acted as a conduit, enabling the hydration and serpentinization of this area.

At the eastern end of the profile, we observe top basement velocities (∼ 5.5 km s^{-1}) resolved in both blocks B3 and B2, east of their interpreted bounding faults, F4 and F3, respectively (arrows ii and iii, Fig. 14e). The velocity in the updip end of the rotated fault blocks increases to values consistent with crystalline basement, indicating that the internal structure of these blocks is resolved to a greater degree. Additionally, there is a shallowing of mantle velocities (∼8.0 km s^{-1}) below continental block B2, which removes an apparent step in these velocities observed in the starting model (arrow iv, Fig. 14e).

4.1.2 Continental fault blocks

The starting velocity model has minimal adherence to the interpreted geological horizons within fault block B4–B7 (Figs 15d–f). Velocity contours cut across reflection horizons obliquely, where they would be expected to run parallel, and no sharp velocity changes are observed laterally across normal faults. Significant improvements are observed in the FWI velocity model (arrows i–xiii in Figs 15g–i), relative to the starting model, with an increased correlation between the velocity field and a number of the interpreted faults and reflection horizons. In some areas, we also observe increased correlation between the velocity model and seismic reflections, which have not been interpreted previously (dashed lines, Figs 15g–i). Particularly good improvement is observed in the internal velocity structure of continental blocks B6 and B7 (arrows i–v, Figs 15g and h, and to a lesser degree B6a and B5 (arrows vi–x,

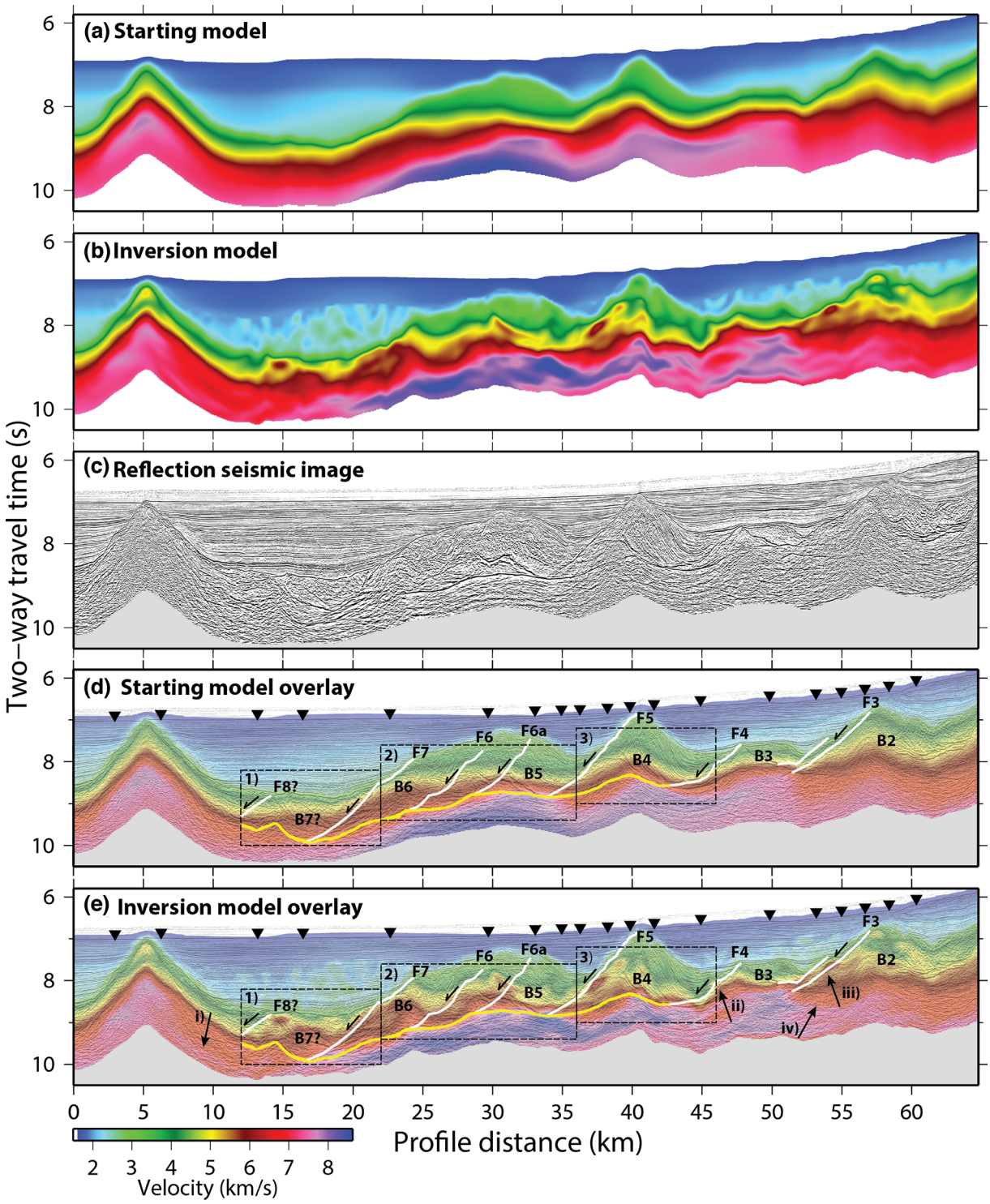

Figure 14. Comparison of large-scale features with seismic reflection imaging. (a) Starting velocity model. (b) Final FWI velocity model. (c) Kirchhoff pre-stack time-migrated multichannel seismic image of inline 420. (d) Reflection image overlain with starting velocity model. (e) Reflection image overlain with FWI velocity model. White lines indicate the location of interpreted normal faulting and the yellow line is the interpreted *S*-reflector. Black upturned triangles indicate the locations of utilized instruments. Dashed black rectangles indicate the zoomed regions illustrated in Figs 4–15. Black arrows indicate regions discussed in the text.

Fig. 15h). In these regions of the model, we see a rotation of the velocity field, particularly at the top of crystalline basement, so that velocity contours run parallel to significant reflections. For example, in block B6 (Fig. 15e), starting velocities at the top of the interpreted crystalline basement of ∼4.55 km s^{-1} on the updip (western) end, and ∼5.95 km s^{-1} on the downdip end (eastern). This gives a velocity difference of ∼1.40 km s^{-1} along a lithological boundary where we would expect to observe a roughly constant velocity. After the inversion, the velocities in these same model locations are now ∼5.35 and ∼5.65 km s^{-1}, updip and downdip, respectively; a velocity

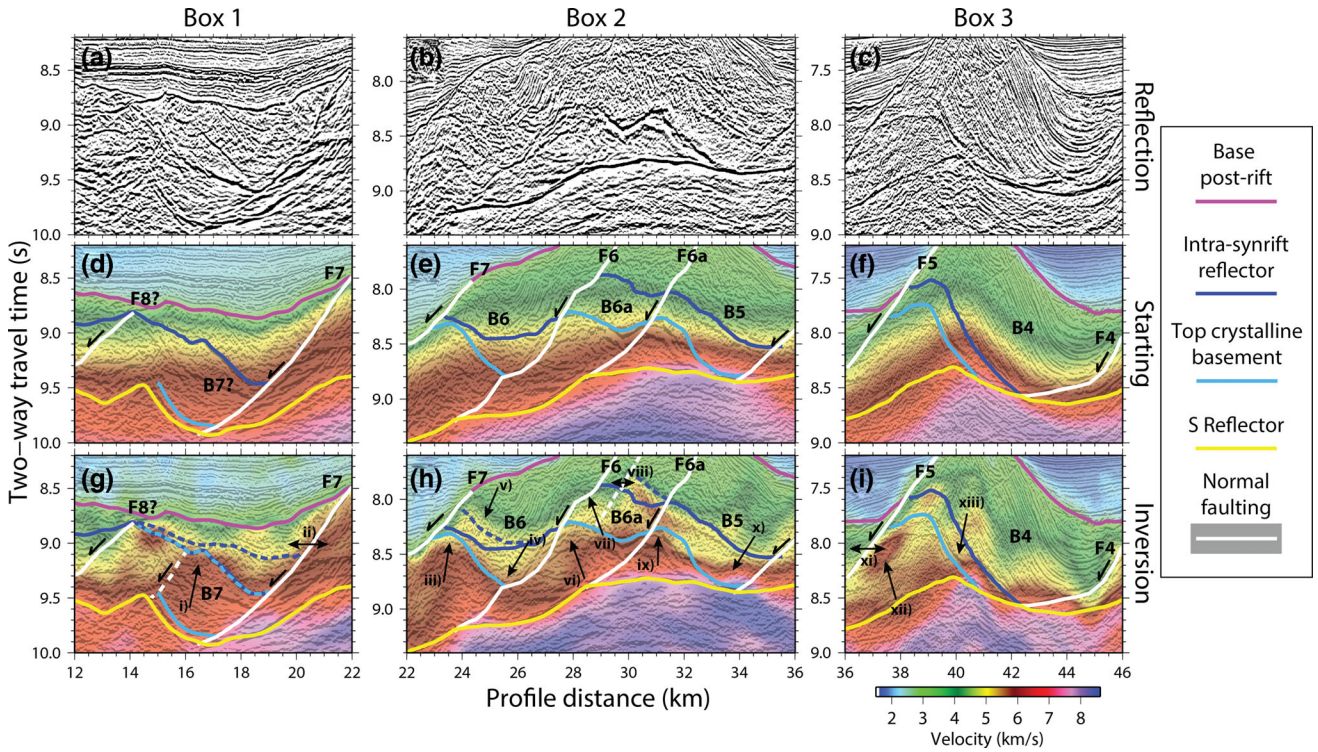

Figure 15. (a)–(c) Sections of interest of the Kirchhoff pre-stack time-migrated multichannel seismic image of inline 420. (d)–(f) Same reflection images as (a)–(c), overlain by the time-converted starting velocity model. (g)–(i) Same reflection images as (a)–(c), overlain by the time-converted final FWI velocity model. Interpreted faults and horizons: white lines indicate normal faulting; yellow lines indicate the *S*-reflector; pink lines indicate the base of the post-rift sediments; dark blue indicate an intra syn-rift horizon and light blue indicates the top of crystalline basement. Black arrows indicate regions discussed in the text. Dashed lines indicate the reinterpretation of faults and horizons, based on the final FWI velocity model.

difference of only $\sim 0.30\,\mathrm{km\ s^{-1}}$ along the same boundary. Similar improvements in the crystalline basement velocities are observed in block B7 (Figs 15d and g), and less substantial improvements are also seen in blocks B6a and B5 (arrows vi and ix, Figs 15e and h).

Despite not resolving constant velocities along the layer boundaries within block B4 (Figs 15f and i), the FWI process has begun to introduce the appropriate higher velocities ($\sim$6.00 km s^{-1}) into the area interpreted as crystalline basement. These velocities are prominently resolved next to the westward fault, F5 (arrow xii, Fig. 15i). The area of high velocity within the crystalline basement of B4 now exhibits a large velocity contrast laterally across normal fault F5, with the syn-rift unit of block B5 (arrow xi, Fig. 15i). We observe a lateral velocity contrast of $\sim 1.70\,\mathrm{km\ s^{-1}}$ over a distance of less than 1.00 km across fault F5, where the starting contrast was previously $\sim 0.75\,\mathrm{km\ s^{-1}}$. This result indicates an increased resolution of the velocity changes across normal faults, which are inferred to have juxtaposed different lithologies against one another. This improvement in the lateral velocity contrast is also observed between the crystalline basement of block B6 and the syn-rift unit of block B7, across fault F7 (arrow ii, Fig. 15g). There is also evidence of a previously unidentified fault within block B6a, between faults F6 and F6a (Fig. 15h). A sharp lateral velocity contrast of $\sim 1.50\,\mathrm{km\ s^{-1}}$ (arrow viii, Fig. 15h), and westward dipping velocity field, highlights a weak reflector which we interpret as a normal fault.

Even though these areas of the FWI model exhibit apparent improvement, there are areas where we now observe velocity patterns which do not match the reflection image and its interpretation. Within fault block B4 (Fig. 15i), a large portion of the unit interpreted as crystalline basement remains unresolved, with uncharacteristically low velocities. There are also areas where we observe a chaotic pattern in the velocities, exhibiting little correlation to imaged sedimentary reflectors. A similar uncorrelated velocity pattern is observed in the sedimentary units of block B5 (Figs 15h and i). A small, and unlikely, circular velocity inversion is observed directly east of fault F8 (Fig. 15g). These areas all appear to be well resolved in the checkboard tests (Fig. 13), which suggests that these artefacts do not arise as a result of the survey geometry. They may instead arise from the presence of out-of-plane arrivals affecting the FWI, and cycle skipping in the longer offset data that is not corrected during FWI (e.g. -14.92 km in Figs 11c and i). While random noise within field data will be attenuated through the FWI process, coherent noise, such as that from multiple energy, can be mapped into false velocity structure (Pratt *et al.* 1998). It is difficult to determine where such artefacts are to be expected, other than using qualitative model assessments, such as comparisons with reflection imaging.

The final velocity model appears to have been resolved well in areas with seismic velocities within the fault blocks of 2.80–5.20 km s^{-1} for the syn- and pre-rift sediments, 5.20–6.50 kms^{-1} for crystalline basement, and 6.50–8.50 km s^{-1} for the uppermost mantle, directly below the *S*-reflector. These typical unit velocities, and their associated boundary velocities, enable us to reinterpret the reflection seismic image. Previous interpretations have failed to identify continental fault block B7 (e.g. Borgmeyer 2010), or have interpreted it to be a completely pre-/syn-rift sedimentary unit, above the *S*-reflector (Fig. 15g). However, seismic velocities indicative of crystalline basement ($\sim$ 6.00 km s^{-1}) allow us to reinterpret the reflection horizons in this fault block. Where previous interpretations had indicated the presence of the intra syn-rift reflector, we

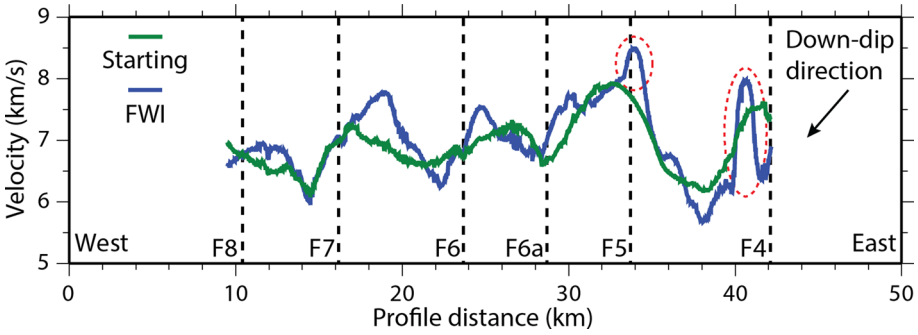

Figure 16. Velocities below the interpreted *S*-reflector (averaged over a 100 ms window). The green line indicates velocities from the starting velocity model and the blue line indicates velocities from the final FWI velocity model. Vertical dashed lines indicate the locations where interpreted normal faults sole onto the *S*-reflector. Red dashed ellipses indicate anomalous features of the inversion model.

now interpret this as the top of crystalline basement, and the intra syn-rift reflector is reinterpreted above, along a reflector near the ~4.90 km s^{-1} velocity contour. We have also reinterpreted the intra syn-rift reflector in fault block B6 (Fig. 15h). Velocities in this unit do not support the reflector pinching out to the west, as originally suggested, but instead suggest that it maintains a consistent thickness, following a consistent velocity of ~4.90 km s^{-1} and matches a prominent reflector in the seismic image. Additionally, the intra syn-rift reflector is reinterpreted between fault F6a and the newly interpreted fault (Fig. 15h).

The interpretation of the smallest continental fault block, B7, agrees with the sequential faulting model, which predicts that the continental blocks decrease in size oceanward. However, the interpretation of previously unidentified normal faulting, combined with the observation of irregular basement and syn-rift velocities, within previously identified fault blocks (see Fig. 15h) indicates that the pattern of deformation within the hyperextended domain is more complicated than that described by the sequential faulting model. These interpretations could suggest that there was an earlier phase of faulting, which has subsequently been overprinted by the large dominant normal faults which are observed in the reflection seismic images. Such interpretations would give favour to polyphase faulting models, which describe complex fault overprinting, and contradict the sequential faulting model.

4.2 *S*-reflector and associated velocities

The *S*-reflector represents a significant velocity contrast between rocks of the lower crust juxtaposed against upper-mantle peridotites which have been serpentinized to varying degrees. Our starting model exhibits a relatively low-velocity contrast across the *S*-reflector, which is the result of the smooth nature of the traveltime tomography modeling. However, we see a sharpening of the velocity contrast over the *S*-reflector in the FWI model, indicating that the velocities directly above and below the fault surface are being resolved to a greater degree. This is particularly well observed below fault blocks B4, B5 and B6a, where the average velocity contrasts (difference between velocities 50 ms above and below the mapped *S*-reflector surface) increase from 0.25, 0.39 and 0.39 km s^{-1}, to 0.50, 0.68 and 0.55 km s^{-1}, respectively. In reality, the velocity contrast across the *S*-reflector is likely to be sharper than that observed in Figs 14(e) and 15(g) and (h), however, the resolution of the FWI is limited by the relatively low inversion frequencies used (3.0–5.2 Hz).

It is difficult to gauge from the 2-D velocity plots whether there has been an improvement in the velocities associated with serpentinization of upper-mantle peridotite along and below the *S*-reflector. The interaction between normal faulting and the *P*-wave velocities below the *S*-reflector is more apparent plotted as velocity against distance. Velocities averaged over a 100 ms window below the mapped *S*-reflector are plotted against the profile distance, for both the starting and inversion velocity model (Fig. 16). The starting model exhibits a general pattern of preferential mantle serpentinization, which is observed as relative decreases in the seismic velocity downdip of normal faults (Davy *et al.* 2016). This trend is particularly evident downdip of faults F6 and F7. However, in this model slight increases in the velocity downdip of faults F5 and F6a can be observed, before the expected velocity decrease. These velocity increases, despite being minor, contradict the hypothesis of preferential hydration and serpentinization of the mantle by normal faulting.

In the same figure, it can be seen that the FWI result has resolved the pattern of preferential mantle serpentinization in greater detail. Decreases in seismic velocity are now seen directly downdip of normal faults, F5–F8 (Fig. 16). This result is more consistent than the starting model with the hypothesis that normal faults act as conduits, enabling the preferential hydration and serpentinization of upper-mantle peridotites below the *S*-reflector (Bayrakci *et al.* 2016; Davy *et al.* 2016). We interpret the consistently low velocities between faults F4 and F5 to be indicative of crustal material, and interpret the *S*-reflector as being intracrustal in this region of the model. Despite this promising result, there are unexpected features in the velocity profile of the FWI model.

We observe two short-wavelength (~2 km) feature which show anomalously rapid change in seismic velocity (highlighted by red dashed ellipsoid in Fig. 16). The most prominent exhibits an increase in velocity of ~1.5 km s^{-1} at 41 km profile distance. This rapid change appears to be particularly anomalous, when compared with the rest of the profile, and differs greatly from the velocity trend in both the starting and inversion models. The other anomalous feature is coincident with fault F5, and reaches the model's maximum allowed velocity of 8.50 km s^{-1}. We expect the velocity of unaltered upper-mantle peridotite to be ~8.00 km s^{-1}, thus making this observation implausible (e.g. Carlson & Miller 2003). These features appear to be artefacts introduced during the FWI process. It is possible that these features arise due to the sparsity of data available in this experiment, or are the result of the FWI process trying to map coherent noise into the velocity model.

Unfortunately, in order to resolve the velocity structure at these depths, we had to include data that were starting to be affected by

coherent multiple noise from the previous seismic shot. Increasing the time between shots would enable greater depth resolution, at the expense of degrading the 3-D reflection image that was the primary aim of the experiment. Ignoring these anomalous short-wavelength features, we can attempt to quantify the levels of observed serpentinization. Relative velocity decreases (from the normal fault to the nearest downdip velocity minima) of ∼0.60, ∼0.60[1], ∼0.70 and ∼1.0 km s^{-1} are observed for faults F5, F6a, F6 and F7, respectively. Using the study of Carlson & Miller (2003), we can approximate the extent of mantle peridotite serpentinization, based on the observed *P*-wave velocities. With the downdip of these faults we calculate the degree of serpentinization, averaged over the resolution length of the FWI, to change from 0 to 20 per cent, 30 to 40 per cent, 30 to 50 per cent and 30 to 60 per cent, for faults F5, F6a, F6 and F7, respectively.

5 CONCLUSIONS

The application of FWI has yielded a clear improvement over traveltime tomography results. From this study we find that:

(1) FWI can be applied to sparse and noisy OBS data in deep-water environments, for the purpose of producing high-resolution velocity models of shallow (< 10 km below seafloor) crustal targets.

(2) The final FWI result is limited by the sparsity of data available, and the presence of coherent noise at longer data offsets.

(3) The final velocity model exhibits a significant increase in resolution within the continental fault blocks of this hyperextended domain. This improvement in the velocity model has enabled the reinterpretation of the reflection seismic image.

(4) Newly interpreted faults, within the existing continental blocks, may provide evidence for an earlier phase of faulting which has subsequently been overprinted by the block bounding normal faults. Such an interpretation would lend support to polyphase models of faulting within the hyperextended domain.

(5) Increased resolution in the seismic velocities below the *S*-reflector has further defined the pattern of upper-mantle serpentinization, a result of preferential hydration by normal faults acting as water conduits. The degree of preferential mantle serpentinization is interpreted to vary between 20 and 60 per cent.

Given a more optimized seismic shooting period, we can expect that the results would have shown an even greater quality. Increasing the time between subsequent seismic shots would allow time for energy of the previous shot to dissipate, reducing the coherent noise in the recorded data and enabling greater depth resolution of the FWI method. We suggest that future marine studies, targeting crustal structure, take into consideration the application of FWI to their proposed data sets. While a higher density of OBS/H is desirable, we have shown that a relatively sparse profile can improve the resolution of traveltime tomography models. This approach will also allow for the improved migration of reflection seismic images, which was not investigated here. There may also be merit in applying the FWI method to existing high-quality 2-D OBS/H data sets where high-quality traveltime tomography models have already been determined.

ACKNOWLEDGEMENTS

We thank the sponsors of the FULLWAVE consortia for support in developing the full-waveform inversion (FWI) software used here. Data acquisition was supported by the US National Science Foundation, the UK Natural Environment Research Council (grant NE/E016502/1) and GEOMAR Helmholtz Centre for Ocean Research. TAM was supported by a Wolfson Research Merit award. Ocean bottom instrumentation was provided by the UK Ocean Bottom Instrumentation Facility and by GEOMAR Helmholtz Centre for Ocean Research. We would like to thank everyone who participated and contributed hard work to the data acquisition, either aboard the R/V Marcus Langseth or the F/S Poseidon. Additionally, we would like to thank the two reviewers, Gail Christenson and Emilie Hooft, who provided excellent feedback which has greatly helped refine the manuscript. The wide-angle seismic data used in this study can be accessed at https://doi.pangaea.de/10.1594/PANGAEA.859069.

REFERENCES

Arnoux, G.M., Toomey, D.R., Hooft, E.E., Wilcock, W.S., Morgan, J., Warner, M. & VanderBeek, B.P., 2017. Seismic evidence that black smoker heat flux is influenced by localized magma replenishment and associated increases in crustal permeability, *Geophys. Res. Lett.,* **44,** 1687–1695.

Bayrakci, G. *et al*,, 2016. Fault-controlled hydration of the upper mantle during continental rifting, *Nat. Geosci.,* **9,** 384–388.

Beslier, M.-O., Ask, M. & Boillot, G., 1993. Ocean-continent boundary in the Iberia Abyssal Plain from multichannel seismic data, *Tectonophysics,* **218,** 383–393.

Boillot, G., Winterer, E. & Meyer, A., 1987. Introduction, objectives, and principal results: Ocean Drilling Program Leg 103, west Galicia Margin, *Proc. Ocean Drill. Program, Initial Reports*, Vol. **103**, pp. 3–17.

Borgmeyer, A.L., 2010. Three-dimensional geometries of rifting on a hyperextended margin-Interpretation of seismic reflection profiles from the Deep Galicia Basin, Iberia, MSc thesis, Rice University.

Brossier, R., Operto, S. & Virieux, J., 2009. Seismic imaging of complex onshore structures by 2D elastic frequency-domain full-waveform inversion, *Geophysics,* **74,** WCC105–WCC118.

Bunks, C., Saleck, F.M., Zaleski, S. & Chavent, G., 1995. Multiscale seismic waveform inversion, *Geophysics,* **60,** 1457–1473.

Carlson, R.L. & Miller, D.J., 2003. Mantle wedge water contents estimated from seismic velocities in partially serpentinizedperidotites, *Geophys. Res. Lett.,* **30,** 1250, doi:10.1029/2002GL016600.

Davy, R. *et al*,, 2016. Continental hyperextension, mantle exhumation, and thin oceanic crust at the continent-ocean transition, West Iberia: new insights from wide-angle seismic, *J. geophys. Res.,* **121,** 3177–3199.

Dean, S., Sawyer, D. & Morgan, J., 2015. Galicia Bank ocean–continent transition zone: new seismic reflection constraints, *Earth planet. Sci. Lett.,* **413,** 197–207.

Dessa, J.X., Operto, S., Kodaira, S., Nakanishi, A., Pascal, G., Virieux, J. & Kaneda, Y., 2004. Multiscale seismic imaging of the eastern Nankai trough by full waveform inversion, *Geophys. Res. Lett.,* **31,** L18606, doi:10.1029/2004GL020453.

Gardner, G., Gardner, L. & Gregory, A., 1974. Formation velocity and density—the diagnostic basics for stratigraphic traps, *Geophysics,* **39,** 770–780.

Jaiswal, P., Zelt, C.A., Bally, A.W. & Dasgupta, R., 2008. 2-D traveltime and waveform inversion for improved seismic imaging: Naga Thrust and Fold Belt, India, *Geophys. J. Int.,* **173,** 642–658.

Jones, C., Evans, M., Ratcliffe, A., Conroy, G., Jupp, R., Selvage, J. & Ramsey, L., 2013. Full waveform inversion in a complex geological setting-a narrow azimuth towed streamer case study from the Barents Sea, in *Proceedings of the 75th EAGE Conference,* Extended Abstracts, doi:10.3997/2214-4609.20130830.

Kamei, R., Pratt, R.G. & Tsuji, T., 2012. Waveform tomography imaging of a megasplay fault system in the seismogenicNankaisubduction zone, *Earth planet. Sci. Lett.,* **317,** 343–353.

Kapoor, S., Vigh, D., Wiarda, E. & Alwon, S., 2013. Full waveform inversion around the world, in *Proceedings of the 75th EAGE Conference,* Extended Abstracts, doi:10.3997/2214-4609.20130827.

Kolb, P., Collino, F. & Lailly, P., 1986. Pre-stack inversion of a 1-D medium, *Proc. IEEE,* **74,** 498–508.

Korenaga, J., Holbrook, W., Kent, G., Kelemen, P., Detrick, R., Larsen, H.C., Hopper, J., Dahl & Jensen, T., 2000. Crustal structure of the southeast Greenland margin from joint refraction and reflection seismic tomography, *J. geophys. Res.,* **105,** 21591–21614.

Lailly, P., 1983. The seismic inverse problem as a sequence of before stack migrations, in *Conference on Inverse Scattering: Theory and Application*, eds Bednar, J.B., Redner, R., Robinson, E. & Weglein, A., *SocIety for IndustrIal and Applied Mathematics,* Philadelphia, PA.

McDermott, K. & Reston, T., 2015. To see, or not to see? Rifted margin extension, *Geology,* **43,** 967–970.

Minshull, T.A., Sinha, M.C. & Peirce, C., 2005. Multi-disciplinary, subseabed geophysical imaging, *Sea Technol.,* **46,** 27–31.

Mispel, J., Houbiers, M., Knudsen, B. & Amundsen, L., 2013. FWI with OBC data from the Mariner Field, UK—the impact on mapping sands at reservoir level, in *Proceedings of the 75th EAGE Conference,* Extended Abstracts, doi:10.3997/2214-4609.20130829.

Morgan, J., Warner, M., Arnoux, G., Hooft, E., Toomey, D., VanderBeek, B. & Wilcock, W., 2016. Next-generation seismic experiments–II: wide-angle, multi-azimuth, 3-D, full-waveform inversion of sparse field data, *Geophys. J. Int.,* **204,** 1342–1363.

Morgan, J., Warner, M., Bell, R., Ashley, J., Barnes, D., Little, R., Roele, K. & Jones, C., 2013. Next-generation seismic experiments: wide-angle, multi-azimuth, three-dimensional, full-waveform inversion, *Geophys. J. Int.,* **195,** 1657–1678.

Mothi, S., Schwarz, K. & Zhu, H., 2013. Impact of full-azimuth and long-offset acquisition on Full Waveform Inversion in deep water Gulf of Mexico, in *Proceedings of the 75th EAGE Conference,* Extended Abstracts, doi:10.1190/segam2013-0102.1.

Operto, S., Virieux, J., Amestoy, P., L'Excellent, J.-Y., Giraud, L. & Ali, H.B.H., 2007. 3D finite-difference frequency-domain modeling of visco-acoustic wave propagation using a massively parallel direct solver: a feasibility study, *Geophysics,* **72,** SM195–SM211.

Operto, S., Virieux, J., Dessa, J.X. & Pascal, G., 2006. Crustal seismic imaging from multifold ocean bottom seismometer data by frequency domain full waveform tomography: application to the eastern Nankai trough, *J. geophys. Res.,* **111,** B09306, doi:10.1029/2005JB003835.

Pérez-Gussinyé, M., 2013. A tectonic model for hyperextension at magma-poor rifted margins: an example from the West Iberia–Newfoundland conjugate margins, *Geol. Soc. Lond. Spec. Publ.,* **369,** 403–427.

Pérez, Gussinyé, M., Ranero, C., Reston, T.J. & Sawyer, D., 2003. Mechanisms of extension at nonvolcanic margins: evidence from the Galicia interior basin, west of Iberia, *J. geophys. Res.,* **108,** 2245, doi:10.1029/2001JB000901.

Pérez, Gussinyé, M. & Reston, T.J., 2001. Rheological evolution during extension at nonvolcanic rifted margins: onset of serpentinization and development of detachments leading to continental breakup, *J. geophys. Res.,* **106,** 3961–3975.

Pratt, R.G., 1999. Seismic waveform inversion in the frequency domain, Part 1: theory and verification in a physical scale model, *Geophysics,* **64,** 888–901.

Pratt, R.G., Shin, C. & Hick, G., 1998. Gauss–Newton and full Newton methods in frequency–space seismic waveform inversion, *Geophys. J. Int.,* **133,** 341–362.

Ranero, C.R. & Pérez-Gussinyé, M., 2010. Sequential faulting explains the asymmetry and extension discrepancy of conjugate margins, *Nature,* **468,** 294–299.

Ratcliffe, A. *et al*,, 2011. Full waveform inversion: a North Sea OBC case study, in *2011 SEG Annual Meeting*, Vol. 30, pp. 2384–2388. Society of Exploration Geophysicists, Expanded Abstracts.

Reston, T.J., 2009. The structure, evolution and symmetry of the magma-poor rifted margins of the North and Central Atlantic: a synthesis, *Tectonophysics,* **468,** 6–27.

Reston, T.J., Leythäuser, T., Booth, Rea, G., Sawyer, D., Klaeschen, D. & Long, C., 2007. Movement along a low-angle normal fault: the S reflector west of Spain, *Geochem. Geophys. Geosyst.,* **8,** Q06002, doi:10.1029/2006GC001437.

Sawyer, D.S., Reston, T., Gussinye, M.P., Zelt, C.A., Austin, J.A., Nakamura, Y., Danobeitia, J. & Cordoba, D., 1997. The Iberia Seismic Experiment (ISE97): MCS reflection profiles, *EOS, Trans. Am. Geophys. Un.,* **78**(1997), p. F468.

Sirgue, L., 2006. The importance of low frequency and large offset in waveform inversion, in *Proceedings of the 68th EAGE Conference,* Extended Abstracts, doi:10.3997/2214-4609.201402146.

Sirgue, L., Barkved, O., Dellinger, J., Etgen, J., Albertin, U. & Kommedal, J., 2010. Thematic set: full waveform inversion: the next leap forward in imaging at Valhall, *First Break,* **28,** 65–70.

Srivastava, S., Sibuet, J.-C., Cande, S., Roest, W. & Reid, I.D., 2000. Magnetic evidence for slow seafloor spreading during the formation of the Newfoundland and Iberian margins, *Earth planet. Sci. Lett.,* **182,** 61–76.

Tarantola, A., 1984. Inversion of seismic reflection data in the acoustic approximation, *Geophysics,* **49,** 1259–1266.

Tarantola, A., 1987. Inverse Problem Theory: Models for Data Fitting and Model Parameter Estimation. *Elsevier,* Amsterdam.

Virieux, J., 1986. P-SV wave propagation in heterogeneous media: velocity-stress finite-difference method, *Geophysics,* **51,** 889–901.

Virieux, J. & Operto, S., 2009. An overview of full-waveform inversion in exploration geophysics, *Geophysics,* **74,** WCC1–WCC26.

Warner, M. *et al*,, 2013. Anisotropic 3D full-waveform inversion, *Geophysics,* **78,** R59–R80.

Warner, M., Umpleby, A., Stekl, I. & Morgan, J., 2010. 3D full-wavefield tomography: imaging beneath heterogeneous overburden, in *Proceedings of the 72nd EAGE Conference,* Extended Abstracts, doi:10.3997/2214-4609.20149944

Williamson, P., 1991. A guide to the limits of resolution imposed by scattering in ray tomography, *Geophysics,* **56,** 202–207.

Wu, R.-S. & Toksöz, M.N., 1987. Diffraction tomography and multisource holography applied to seismic imaging, *Geophysics,* **52,** 11–25.

Zelt, C.A. & Barton, P.J., 1998. Three-dimensional seismic refraction tomography: a comparison of two methods applied to data from the Faeroe Basin, *J. geophys. Res.,* **103,** 7187–7210.

Zelt, C.A., Sain, K., Naumenko, J.V. & Sawyer, D.S., 2003. Assessment of crustal velocity models using seismic refraction and reflection tomography, *Geophys. J. Int.,* **153,** 609–626.